

N O T I C E

THIS DOCUMENT HAS BEEN REPRODUCED FROM
MICROFICHE. ALTHOUGH IT IS RECOGNIZED THAT
CERTAIN PORTIONS ARE ILLEGIBLE, IT IS BEING RELEASED
IN THE INTEREST OF MAKING AVAILABLE AS MUCH
INFORMATION AS POSSIBLE

DRA

Y (3)

PLANETARY SCIENCE INSTITUTE

(NASA-CR-162500) COLLISIONAL AND DYNAMICAL
PROCESSES IN MOON AND PLANET FORMATION
Semiannual Report, 23 May - 22 Nov. 1979
(Planetary Science Inst., Tucson, Ariz.)
106 p HC A06/MF A01

N80-12979

CSCL 03B G3/90

Unclassified
46220



COLLISIONAL AND DYNAMICAL PROCESSES
IN MOON AND PLANET FORMATION

Semi-Annual Report

NASW-2909 Mod 4

May 23, 1979 -- November 22, 1979

Submitted to: Code SL
NASA Headquarters
Washington, D.C. 20546
Attention: Dr. William Quaide

by: The Planetary Science Institute
2030 East Speedway, #201
Tucson, Arizona 85719

SAI - 1-141-00-633-03

This progress report describes work accomplished during the first six months of the current contract period (May 23 - November 22, 1979). Progress has been made on the following topics, for each of which a technical report is appended to this report:

- B.1 Current Progress with the Numerical Model of Planet Growth
- B.2 Experimental Studies of Collisions
- B.3 Hydrodynamic Code Collision Calculations
- B.4 Orbital Element Changes Due to Gravitational Scattering
- B.5 Validation of Mass-Shifting Algorithm
- B.6 Inclination-Type Resonance in a Dissipative Medium
- B.7 Theory of Rotations
- B.8 Origin of Asteroids: Velocity Pumping by Large Jupiter-Scattered Planetesimals

Most of the above work was accomplished during the period May - July.

More recently, Hartmann has developed a methodology to evaluate the rate at which megaregolith increases its depth d as a function of total accumulate number of impacts on an initially smooth, coherent surface. This methodology involves tabulating the percentage of surface covered by craters penetrating deeper than depth d . This relation was then combined with the time behavior of early lunar cratering (Hartmann, et al., Basaltic Volcanism Study Project, Chapter 8, in preparation) to give the megaregolith depth on any rock surface formed (i.e., solidified)

at time t during the early history of the Moon. This rate of destruction of rocky crust can be compared with rates of formation of rocky crust by solidification of the magma ocean, to show how early crustal structure evolved on planet surfaces as a result of accretionary cratering (see Figure 1).

Results of Hartmann's work were presented at the Lunar Highlands Conference, November 1979 (See Appendix Q.1) and a paper is being prepared for those conference proceedings. Recent results on the planet building process were also presented (by Greenberg) at the DPS meeting in St. Louis (see Appendix Q.2).

FIGURE 1: Three stages of lunar surface evolution identified from quantitative models of megolith formation rate and magma ocean pooling rate. In the chaotic pre-crustal stage, the cratering is intense enough to penetrate through lithosphere and mix ejected fragments with molten magma. In the second, crust-forming stage, upper layers of crust are pulverized into megaregolith (resetting isotopic clocks?), but igneous cumulate crust can begin to form at a depth sufficient to be shielded from cratering. This is likely to be tens of kilometers deep. Flows on surface during this stage (4.3 to 4.0 Gy ago?) would be pulverized. In final stage, cratering has dropped to rate where surface flows of plausible thickness (few 10^2 m) would not be completely destroyed. Their lower layers would thus serve as a source for rock samples. This stage (hence datable rock samples) would be younger than 4.0 Gy old.

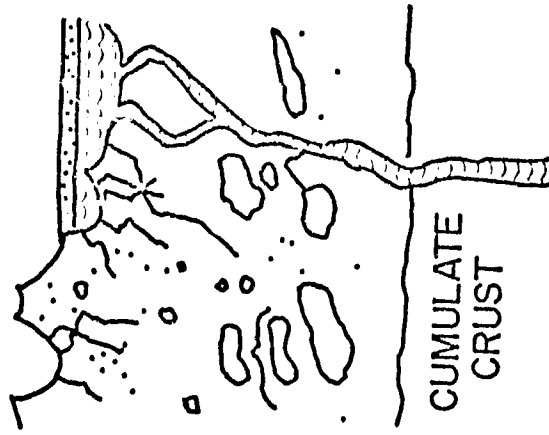
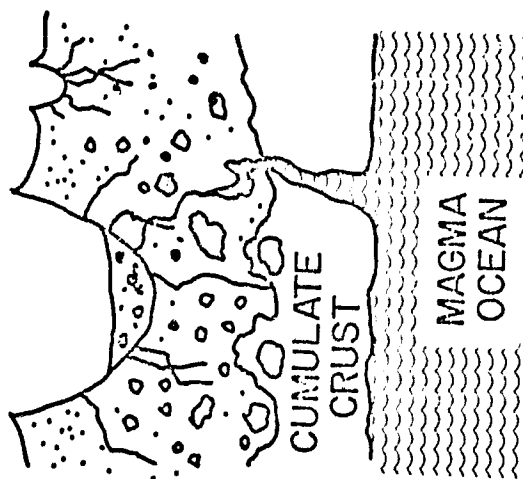
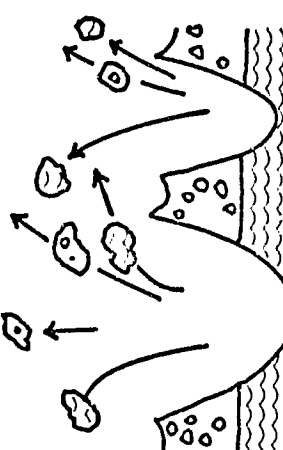
LOCAL MATERIAL (BULK)
60 % ♀ PLANETESIMALS
37 % ♂ PLANETESIMALS
3 % ♂ PLANETESIMALS

CHONDRITIC + CARBONACEOUS CHONDRITIC MATERIAL

- LITHOSPHERE $\geq 100\%$ PENETRATED BY IMPACTS
- MAGMA & ACCUMULATE ROCK MIXED IN MEGAREGOLITH
- LITHOSPHERE TOO THICK TO BE 100% PENETRATED BY IMPACTS
- UPPER MEGAREGOLITH INTENSELY GARDENED
- FLOWS $\leq 1\text{ KM}$ THICK DESTROYED
- CUMULATES AGGREGATE AT DEPTH
- FLOWS $\geq 100\text{ m}$ THICK NOT DESTROYED
- REGOLITH FORMS ON FLOW SURFACES
- MEGAREGOLITH SEVERAL KM DEEP

ORIGINAL
OF POOR PAGE IS
QUALITY

FORMATION



4.5

TIME (Gy BEFORE PRESENT)

4.0

APPENDIX B

RECENT RESULTS AND CURRENT RESEARCH

Contents

- B.1 Current Progress with the Numerical Model of Planet Growth
- B.2 Experimental Studies of Collisions
- B.3 Hydrodynamic Code Collision Calculations
- B.4 Orbital Element Changes Due to Gravitational Scattering
- B.5 Validation of Mass-Shifting Algorithm
- B.6 Inclination-Type Resonance in a Dissipative Medium
- B.7 Theory of Rotations
- B.8 Origin of Asteroids: Velocity Pumping by Large Jupiter-Scattered Planetesimals

APPENDIX B.1

CURRENT PROGRESS WITH THE NUMERICAL MODEL
OF PLANET GROWTH

APPENDIX B.1CURRENT PROGRESS WITH THE NUMERICAL MODEL OF PLANET GROWTH

Our numerical model serves as a central focus for our multi-disciplinary study of planet growth. As we make progress in the various technical issues related to the main problem, we continue to use those results to update and improve our numerical simulation. The model provides insight into the interactions of various processes which are likely to have operated at that time.

The major new mechanism that has been incorporated into our simulation in the past few months is gas drag. Before our original simulation was constructed, one might have reasonably imagined that most primaeval gas had been removed before the epoch of collisional accretion began. However, our results (cf. Greenberg *et al.*, Icarus 35, 1, 1978) have shown that substantial growth may have occurred in only a few 10^4 yr. It thus became less easy to believe that gas had been removed before this growth, and it became important that we incorporate gas drag. From the analysis of Adachi *et al.* (Prog. Theor. Phys. 56, 1756, 1976) and following the notation of Weidenschilling (MNRAS 180, 57, 1977):

$$\frac{de}{dt} = \frac{(2g/\Delta g)e}{t_e} \left[.77e + .64i - \frac{\Delta g}{2g} \right]$$

$$\frac{di}{dt} = \frac{(g/\Delta g)}{t_e} i \left[.77e + .85i - \frac{\Delta g}{2g} \right]$$

$$\frac{da}{dt} = \frac{-2a}{t_e} \left[.97e + .64i - \frac{\Delta g}{2g} \right]$$

where

$$\Delta g = - \frac{nRT}{\mu r} < 0$$

r = distance from sun

$P \propto r^{-n}$ with $n \sim 3.5$

μ = molecular wt. of gas ~ 2.25

R = gas constant

T = temp. $\sim 300^{\circ}\text{K}$

g = solar gravitational acceleration

also t_e is the e-folding time for velocity change due to gas drag. For large Reynolds numbers (applicable if planetesimals are $\gtrsim 10$ m in diameter),

$$t_e = \frac{3D\rho}{\rho_g \Delta V}$$

where

D = planetesimal diameter

ρ = planetesimal density

ρ_g = gas density $\sim 10^{-9}$ gm/cm³ in our nominal model

$$\Delta V = V_{\text{Kepler}} - V_{\text{gas}} = - \left(\frac{\Delta g}{2g} \right) V_{\text{Kepler}}.$$

Thus the gas acts to damp random motion (e and i). But, by introducing a radial drift (da/dt) that varies with body size, it introduces a new source of relative velocity. Values of da/dt for our nominal gas density range from 10^3 cm/sec for a 10 m body to only 10 cm/sec and less for a km or larger body. The numerical simulation program has been modified to include this differential radial drift in the computation of relative velocities. The relative velocities in turn may govern both impact velocities and gravitational stirring. In principal, gravitational interactions can convert radial drift into increased random motion. However, so far in application to our program (cases to be discussed in detail below), conditions have been such that gas drag has primarily damped random motion, rather than stirred it.

A great deal of effort has been expended in making a number of other modifications to our code that improve our confidence in its validity. We find that such changes have

had negligible effects on previously published results. Nevertheless, continued checking and validation of our code is important if we are to ensure that it in fact simulates the physical processes that it is supposed to model.

One such change was required when we found irregularities in the behavior of the inclination of the largest body. The change in each time step, though small, was the difference between a large gravitational stirring increase and a large collision damping effect. For this and other reasons, a numerical procedure had to be developed to avoid loss of precision due to round-off errors.

Another problem was that under certain conditions, we found unaccounted-for changes in total system mass of a few percent. After considerable effort, we found and corrected several minor "bookkeeping" errors, so now mass is conserved to 8 figures.

We also modified our algorithm for shifting bodies into an adjacent size bin as their masses gradually change due to cratering erosion or accretion. Previously, we computed the number of particles shifted out of the bin and added an appropriate number to the adjacent bin so as to conserve mass. We now compute the total mass of particles shifted and adjust numbers in both bins to account for the mass shift. This is

more meaningful physically, although both methods would be equivalent for infinitesimal bin-widths. Use of the new algorithm does not change any previously reported results, but it gives us greater confidence in the continuation of growth to larger bodies to be discussed below. See also Appendix B.5 for discussion of continuing work in the validation of our numerical methods.

As we shall show, the general conclusions of our earlier work (cf. Greenberg *et al.*, Icarus 35, 1, 1978) still hold given the program modifications discussed above. Briefly, those conclusions were that 500 km bodies can grow from a swarm of km bodies in only $\sim 2 \times 10^4$ yr. At the time they grow, most of the mass remains in km size bodies. In accordance with the theory of Safronov (1972, NASA TT F-677), the random relative velocities remain small, on the order of km bodies' escape velocities. We stopped our runs at this point because we felt random eccentricities were so small compared to the "Keplerian" accretion annulus of the largest body that our computation of collision probabilities was invalid. Now we are extending our simulations forward in time to investigate evolution in a later stage of the growth process than had been considered before. A critical scientific question to be answered by extension to later stages (cf. Greenberg *et al.*, in Asteroids, T. Gehrels, ed., in press; Greenberg, Appendix A.2) is whether an equilibrium condition of the type assumed by Safronov (most mass in largest bodies)

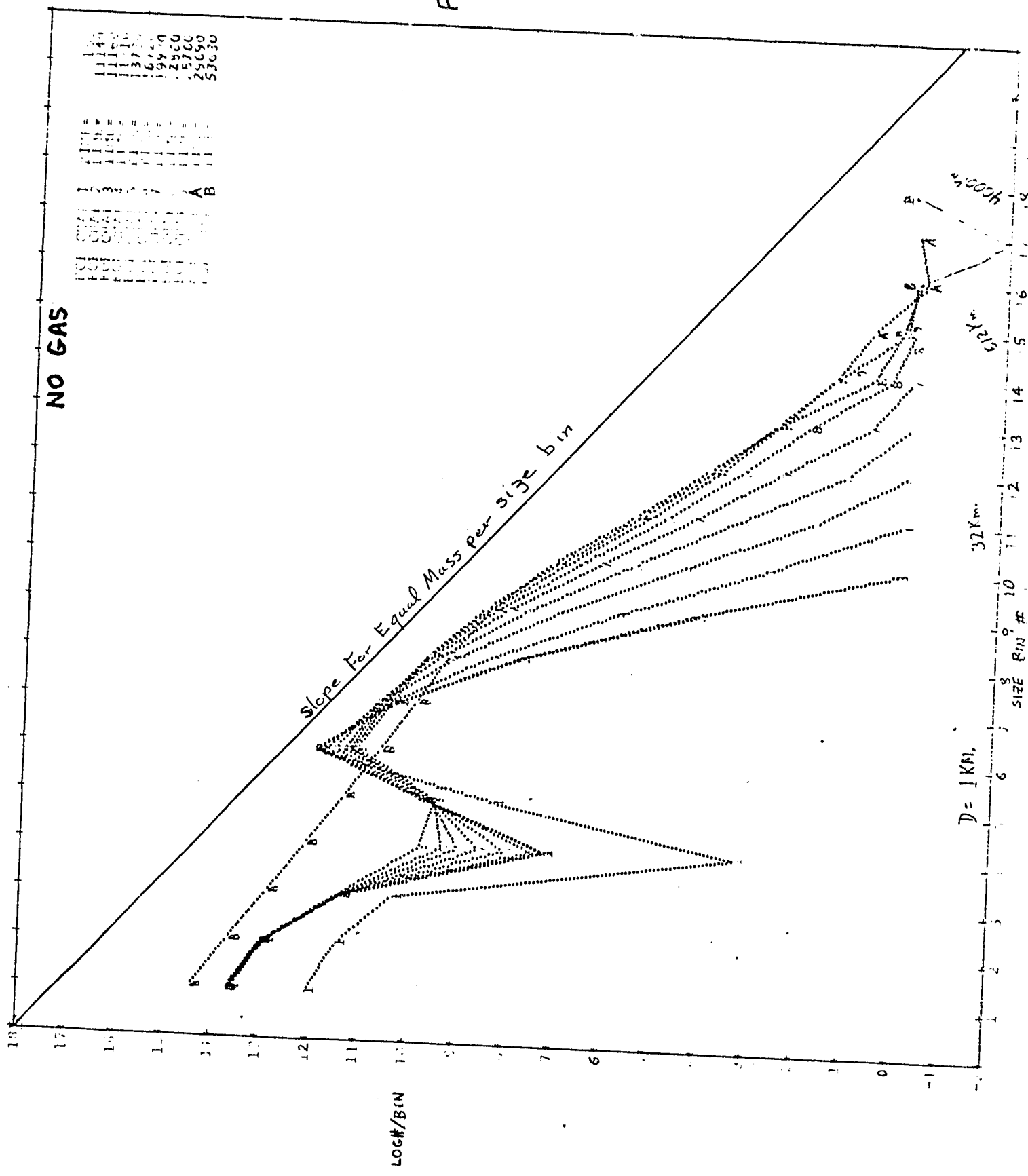
may have held during most of the growth period, or whether the "disequilibrium" situation, found by us in the early stage, persisted throughout much of the growth process. The answer to this question has implications regarding the size of the largest late-stage planetesimals and in turn regarding several observable properties of the current solar system (cf. Greenberg, Icarus, in press, and Appendix B.1).

We now believe that we can extend our simulation past the epoch discussed in our earlier reports and that we were too conservative in stopping our runs when we did. As Kaula (1979, preprint) has pointed out, although we found the largest bodies' orbits to be nearly circularized, the random motion of the smaller bodies, which dominated the population, was considerably greater. So our computation of the interaction of the largest bodies with the bulk of the population was still valid. Furthermore, as we shall show, it remains valid because the velocities increase sufficiently as the largest bodies grow to several thousand km diameters.

Now we examine the results of several recent numerical experiments. First consider an experiment with no gas, and with the "intermediate material" and initial conditions defined by Greenberg et al. (1978) (throughout this discussion the reader's familiarity with that paper will be assumed). The size distribution evolution is shown in Figure 1. When the first 500 km

B.1.7

Fig. 1



body is produced, eccentricities and inclinations of the bulk of the population are a few 10^{-4} , large enough that we can continue the evolution as suggested by Kaula's comment. As the largest body grows to almost 4000 km diameter, typical e 's and i 's are $\approx 2 \times 10^{-3}$. While these increased velocities accompany the growth of the largest body, they are probably not due to the effects of the largest body. Rather, they are due to the shifting of the mass peak in the size distribution from 1 km towards larger values. Towards the end of the period studied, the largest body begins to contain a substantial fraction of the total system mass, as it would in Safronov's equilibrium condition. However, it has already begun "runaway" growth and is effectively detached from the continuous size distribution, so it cannot effectively influence relative velocities (cf. Appendix A.1). Safronov's condition is not achieved at this point. By the time the 4000 km body is produced, the smaller end of the distribution has become linear (a power law). Moreover, relative velocities are so high that bodies up to ≈ 30 km are comminuting one another so that nearly half the mass of the system has been processed into small particles below the size range followed in our numerical model. In reality, one might imagine a power law distribution extending down to such size (a crystal size or a few mm?) that particles' strengths are larger than we have assumed. There

would be a spike in the distribution as the comminuted pieces pile up at that size. This material might experience substantial radial motion due to drag (radiation or gas) and spiral out of the zone under study. But presumably it would be replaced by similar material moving in from an adjacent zone. (We will give more rigorous consideration to that idea.) The small particles would be an additional source of material for accretion by the largest bodies, so the runaway growth found in this experiment is probably an underestimate.

There is a strong indication that Safronov's equilibrium condition may never be reached. Implicit in his work, and explicit in recent publications (Safronov, 1979, preprint) is the idea that the largest bodies are all nearly the same size, as well as containing most of the mass of the system. Schematically, he assumes a size distribution (over the region which finally feeds a planet) to look like Figure 2 over a time scale 10^8 years:

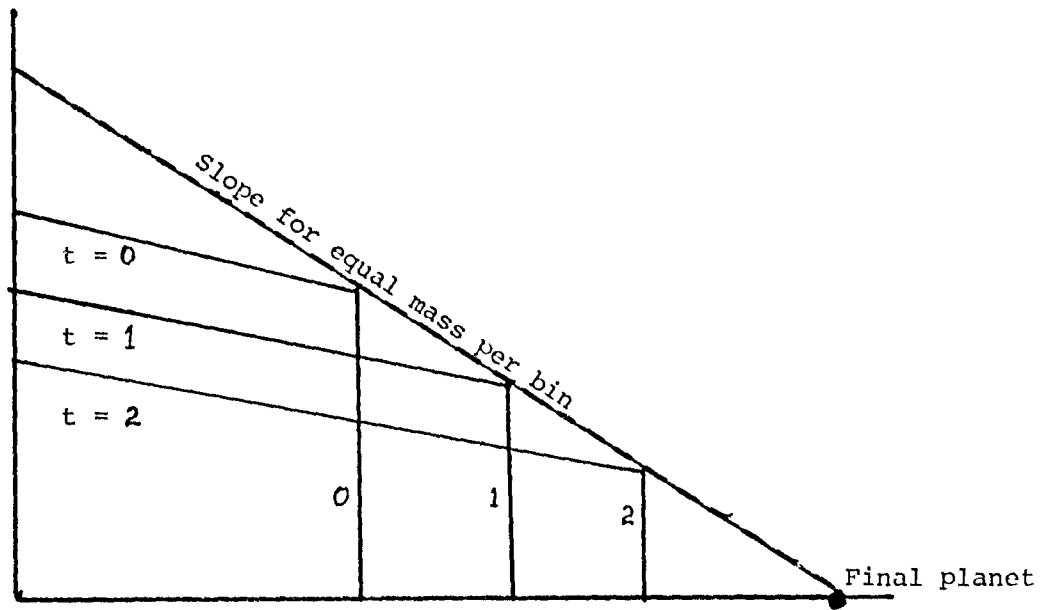


FIGURE 2

In fact, we find a very different situation which can be summarized schematically as well:

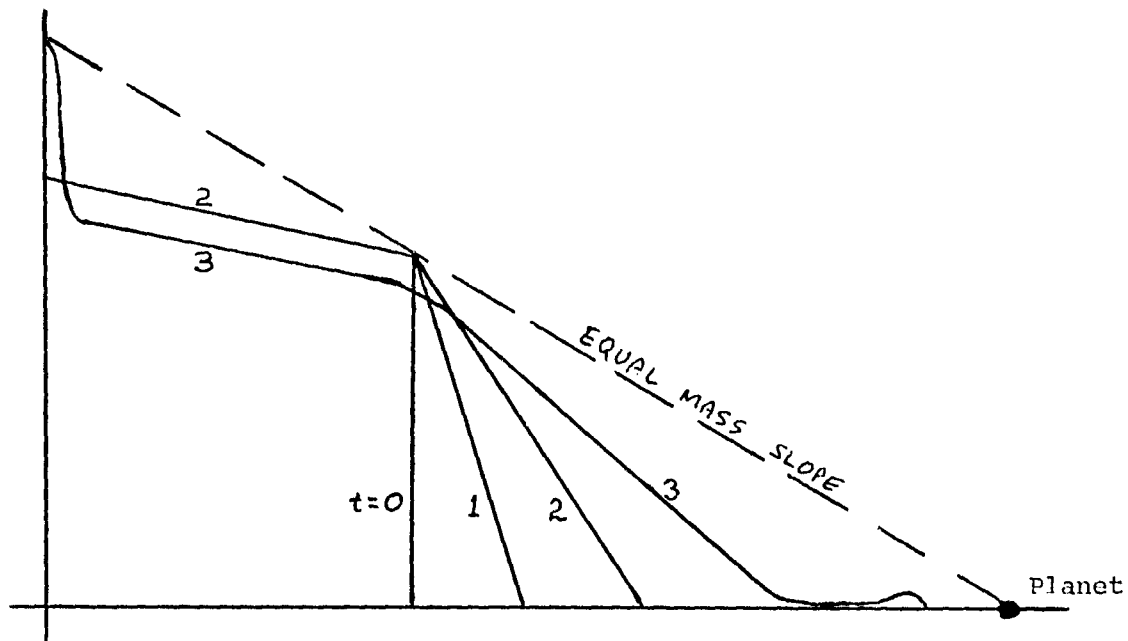


FIGURE 3

Most of the mass stays in small bodies throughout much of the growth, and may even be concentrated into dust particle sizes. Planetesimals random relative velocities stay very low compared to the escape velocity of the largest body. The largest bodies begin to contain a substantial portion of the total mass only after runaway growth of the very largest has begun. There seems to be no prospect for Safronov's equilibrium condition to be reached.

Planetesimals destined to grow into full-sized planets seem to be selected by this runaway process within a few 10^4 yr of our initial state. Conceivably, such multi-thousand-km bodies emerged from the size distribution, conserved their identities and evolved by a wide range of dynamical, geophysical and geochemical processes into the planets we know today. Alternatively, a subsequent period of collisional and gravitational interactions amongst large bodies (cf. Cox et al., *Icarus* 34, 415, 1978) may have interrupted any continuity of identity from the first products of runaway through the final planets. A great deal more research will need to be done on late stage processes before such issues can be resolved.

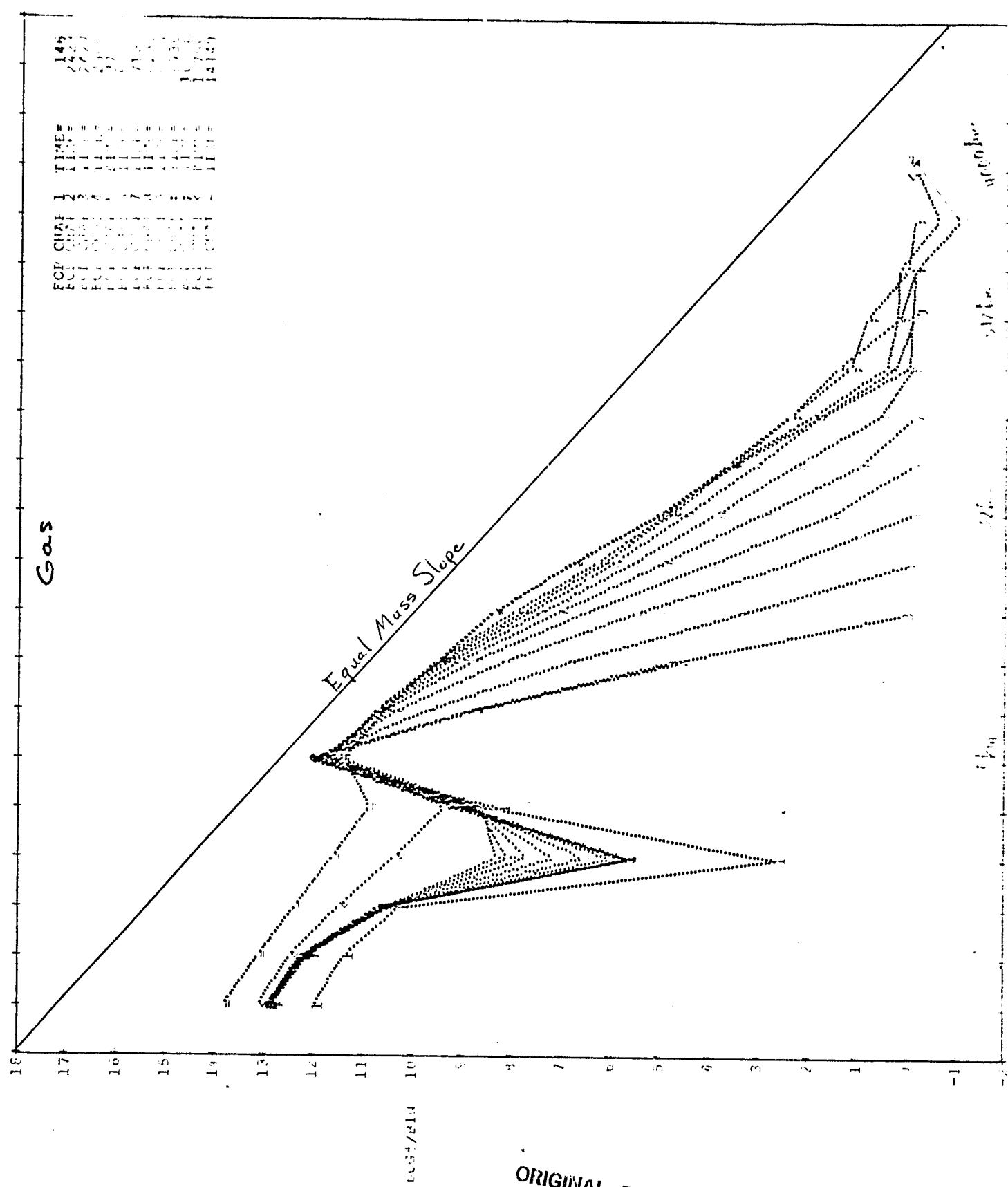
One potential shortcoming of our model is that the computed random velocities represent values averaged over all planetesimals of a given size whether or not they are in the "feeding zones" of the largest body. Presumably, in the

feeding zones velocities would be considerably higher, perhaps giving local satisfaction of Safronov's assumption. Greenberg (1979, Appendix A.2) gives an argument against that possibility. Certainly, we cannot conclude that runaway growth always occurs, rather than Safronov's scenario, until the full range of possible parameters and mechanisms has been explored.

For example, consider how the numerical results are changed if we include gas as per the algorithm described above. The results of this experiment are shown in Figure 4. The basic results are quite similar to the previous case. Relative velocities of planetesimals are somewhat lower, yielding a 500 km body at $t = 9000$ yr. Characteristic e 's and i 's are about 10^{-4} at that time. By the time (5000 yr later) a 4000 km body is produced, velocities are an order of magnitude greater. Velocities remain low enough that only $\sim 1\%$ of the mass has been comminuted out of the system. Most of the mass is in the 4000 km body, and runaway growth seems to be underway. Velocities are low in accordance with Safronov's analytical work on relative velocities, for such a size distribution. But the low velocities and the runaway growth are in gross violation of the assumed conditions for his planet growth scenario.

We have searched for a way to obtain Safronov's conditions.

FIG. 4



For example, we note that Experiment No. 4 of Greenberg et al. (1978), which uses parameters appropriate for a "weak material with low debris velocity," seems to be progressing toward a state consistent with Safronov's assumptions. At least the mass peak in the distribution is moving up in size almost as fast as the largest body grows, and velocities are considerably higher than for intermediate materials. We suspected that continuation of that experiment might lead to Safronov's condition.

The results of continuing that experiment, Figure 5, while somewhat different in detail than the results of other experiments (Figs. 1 and 4) lead to the same general conclusions. The largest body reaches a size somewhat larger than 4000 km and e's and i's are ~ 0.02 . Despite the fact that relative velocities of planetesimals are high compared to velocities in earlier experiments, the comminution of significant mass out the small end of the distribution doesn't begin until after the largest body reaches 4000 km. This is because so much of the mass peak is shifted up to sizes which are immune to great comminution until after e and i become ~ 0.02 . After 4.5×10^5 yr about 1/3 of the mass has been comminuted out, but long before this, runaway growth has set in, with a ~ 6000 km (Mars-sized) body produced.

We are also considering whether the addition of gas combined with varying material properties might give the Safronov equilibrium condition. For example, Figure 6

FIG. 5

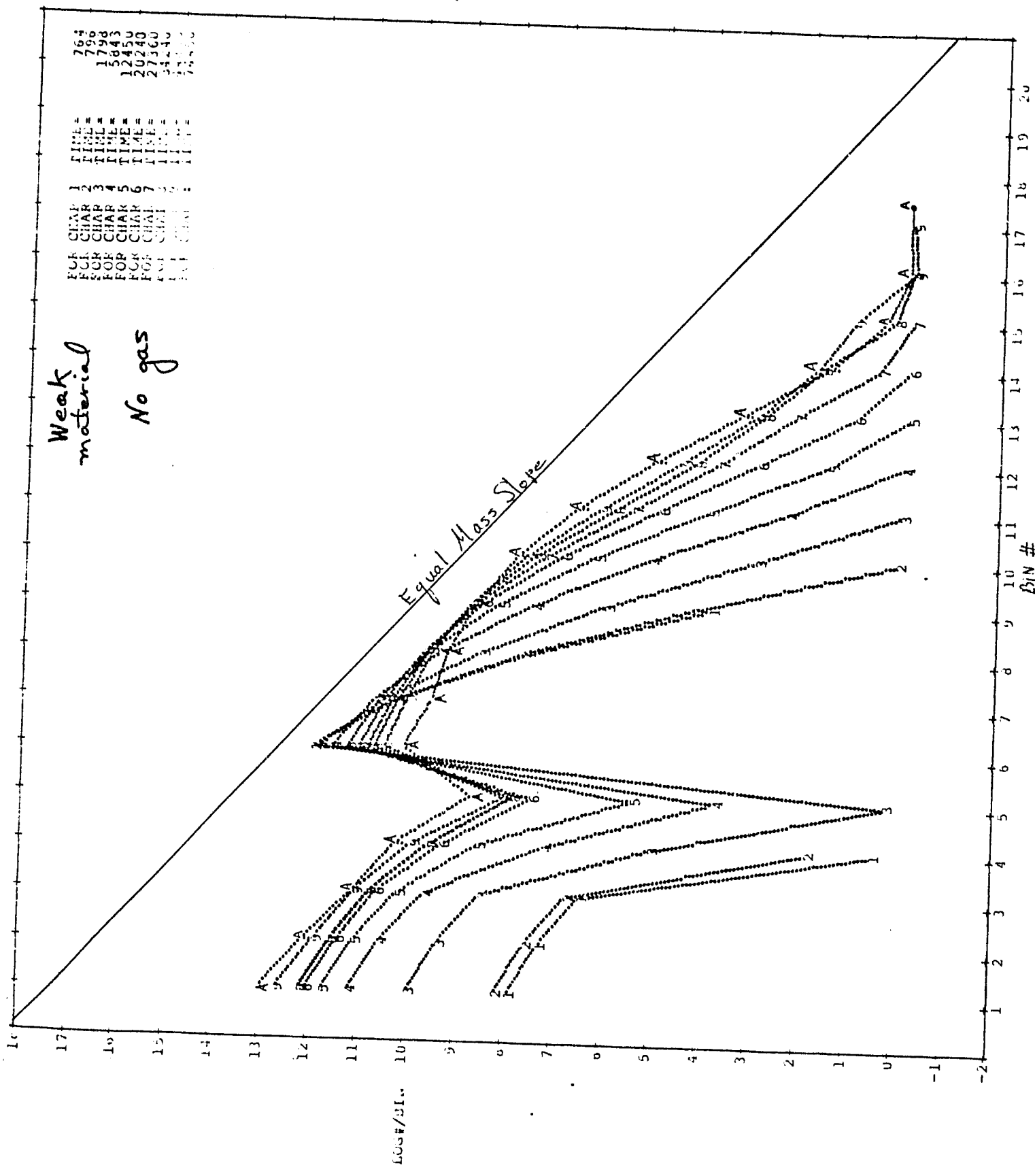
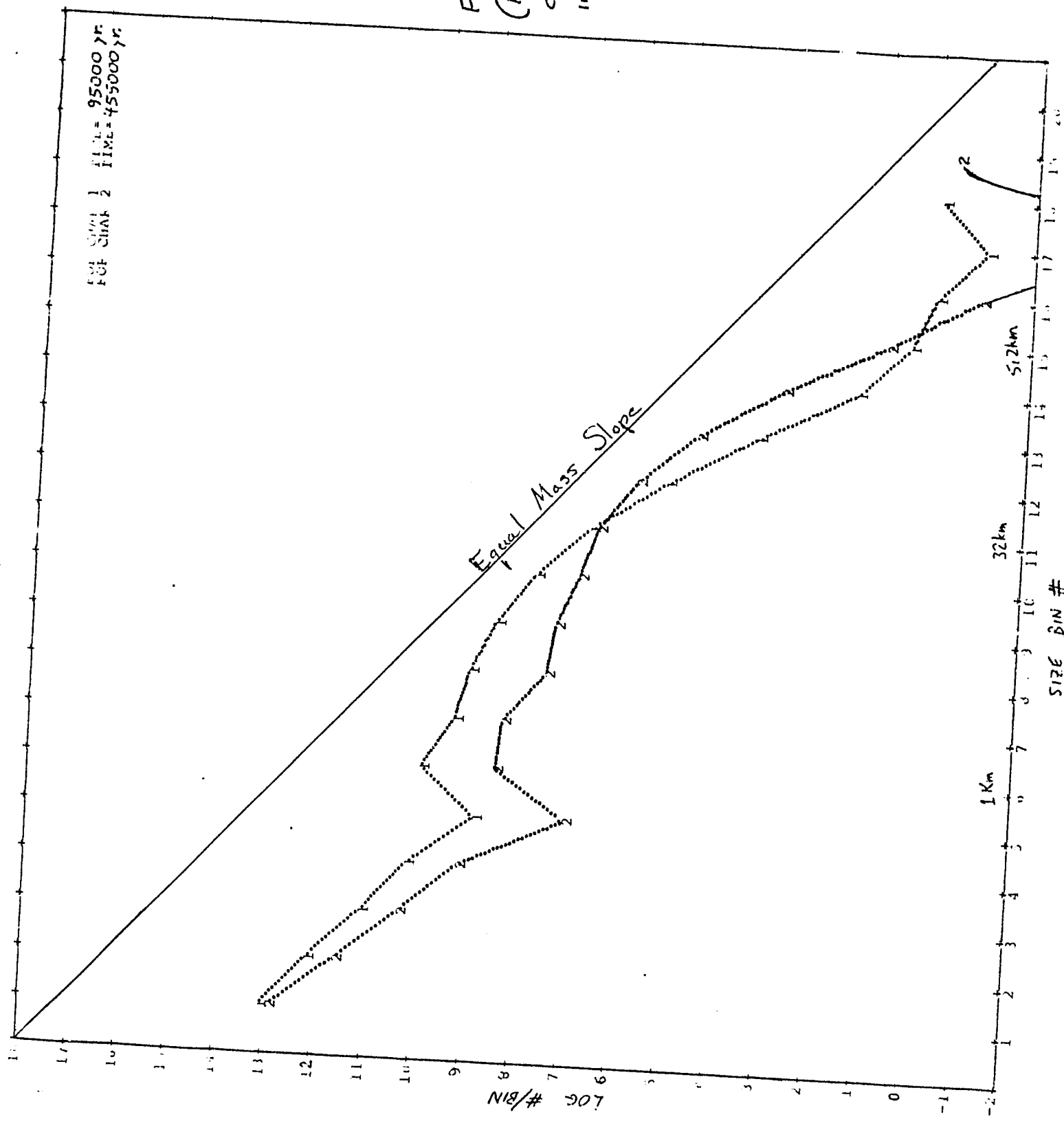
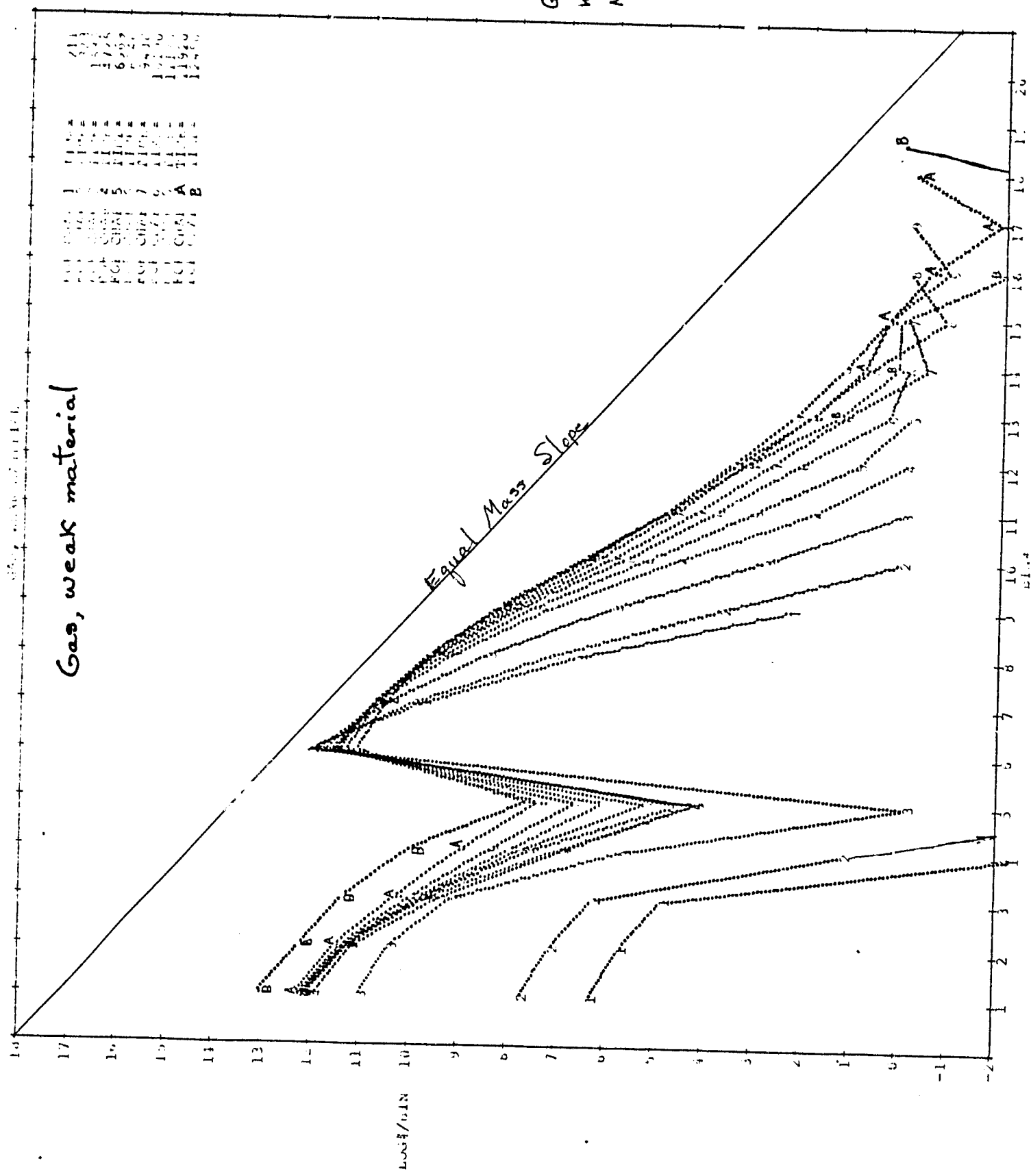


FIG. 5a.
(Fig. 5
continued
in time)



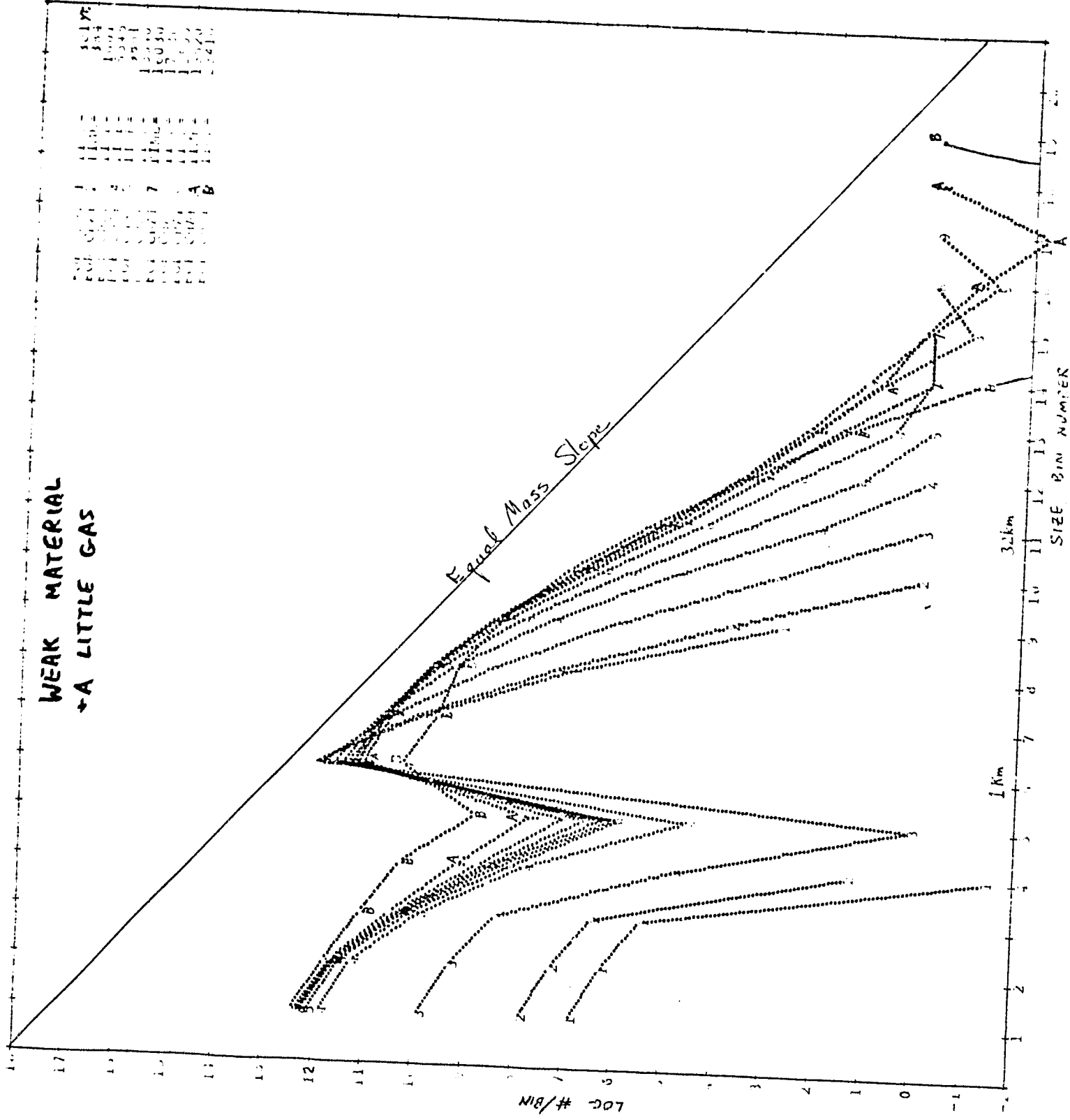


shows a case with gas and the weak material of the previous case. Velocities are about half of what they were, the peak on the continuous portion of the distribution stays near 1 km, and little comminution occurs. Runaway has begun. Figure 7 shows a case between that of Figures 5 and 6: same material but less gas ($t_e = 3 \times$ previous case). Results are similar.

We conclude that, while we cannot now definitively answer the questions that we have posed about the later stages of planet growth, every indication from our work to date is that runaway growth begins at an early stage and that Safronov's assumed equilibrium condition is never reached.

**WEAK MATERIAL
+ A LITTLE GAS**

FIG. 7
WEAK
MATERIAL,
 $\frac{1}{3}$ GAS



APPENDIX B.2

EXPERIMENTAL STUDIES OF COLLISIONS

EXPERIMENTAL STUDIES OF COLLISIONSAmes Vertical Gun

Dr. Hartmann completed a highly successful 8-day run of experiments at the Ames Vertical Gun facility in June 1979. This was the first experimental run since the facility reopened after about two years of inactivity. Dr. Hartmann obtained collision and impact data in the hitherto-unstudied velocity range around $v = 100$ to 150 m/s using an air gun designed by the Ames staff for these experiments. Data on collision outcomes are needed at these v 's and up to some 10^3 m/s, where data were gathered by Gault *et al.* (1963).

Films and sample measurements were obtained at Ames which will give data on the following:

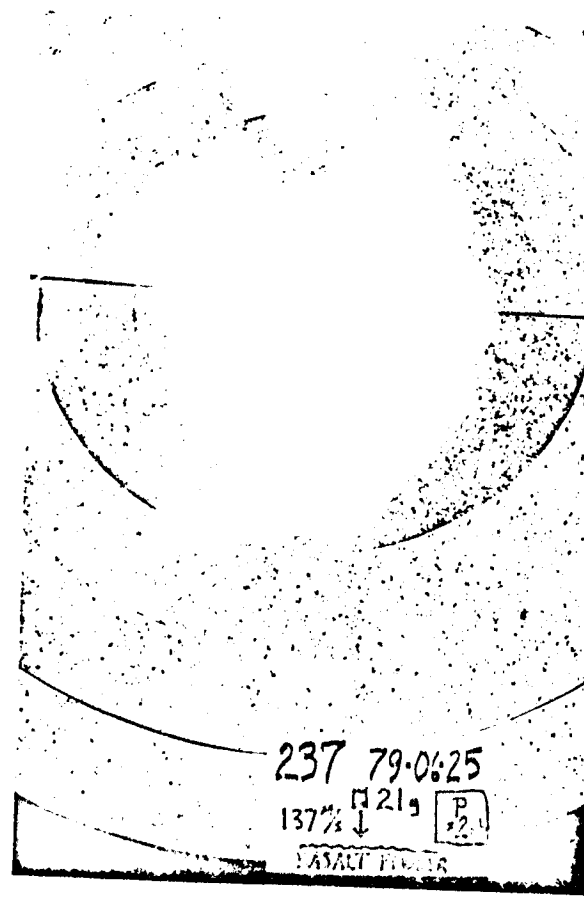
- Ejecta velocities for basalt rock collisions at about 100 - 150 m/s.
- Ejecta velocities for collisions of artificial rock aggregates at velocities about 10 to 150 m/s.
- Ejecta velocities for material blasted out of powdery regoliths in vacuum at impact velocities around 100 - 150 m/s
- Size distributions of fragments in the first two cases.

All of these data, when reduced, will be used for refining our computer modeling of collision events. The only published data on these subjects refers to collisions at less than

60 m/s, or greater than about 1000 m/s. Reduction of the data will be pursued during the current year.

Three examples of results will be discussed here to illustrate progress. First, Figure 1 is a photograph showing the result of firing a 21 g projectile at 137 m/s into a basalt powder (somewhat coarser than lunar regolith; powder size distribution was measured by sieving) in a near vacuum at 2 mb pressure. Note the ray patterns, similar in plan to those on the moon. Cardboard rings were used to collect and weigh ejecta at various annular distances. Films of such experiments at about 2000 frames per second give measures of trajectories of ejecta particles. Trajectory and mass measures will give velocity distributions of ejecta. These should give the first reliable data on mass gain versus mass loss in modest-velocity collisions among planetesimals of different sizes. Some previous estimates of such phenomena relied on extrapolations of much higher-speed collision data, such as pioneering data of Gault and others at around 6 km/sec.

Second, Figure 2 shows the size distributions measured from two similar collisions of 21 g and 166 g projectiles into roughly 3000 g artificial rock aggregate targets in which the typical mass of the constituent grains was about 0.2 g. The figure shows that the mass distribution was about $N \propto m^{-0.9}$, which is consistent with the distributions found during breakup of solid rock targets, showing that the same fragmentation



ORIGINAL PAGE IS
OF POOR QUALITY

FIG. 1

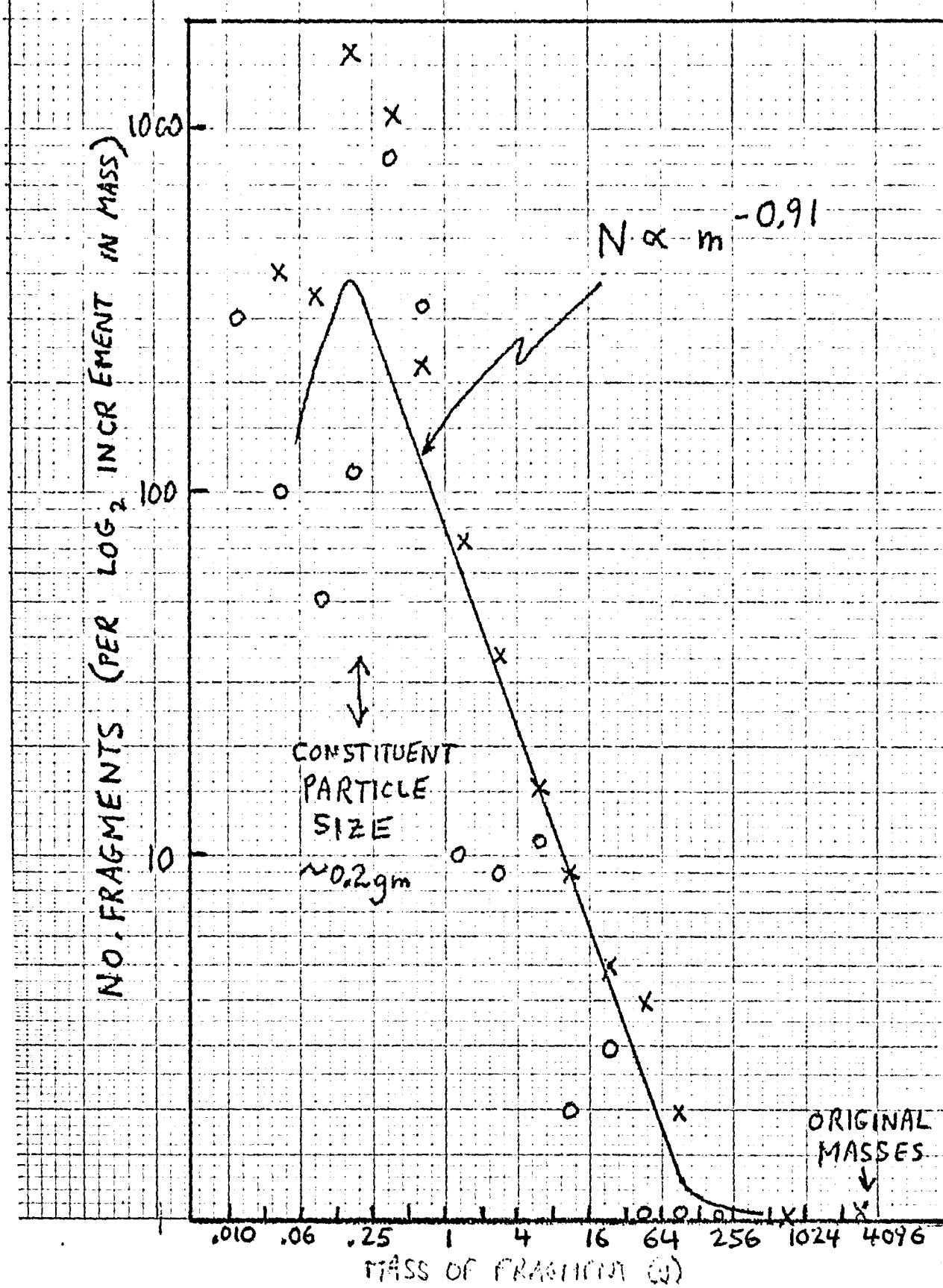


FIG. 2

algorithms can be used to represent these materials. The maximum in the size distribution falls at about the size of the original constituent grains, whose bonding into the aggregate had weaker strength than the grains themselves. This gives a handle on the mode of breakup of early planetesimals that may be loose aggregates of small particles. Another feature of the graph is the relation of the original masses, largest fragments, and other fragments. This bears some superficial similarities to observed size distributions of small-body populations in the solar system today.

Third, Figure 3 shows an updated approach to measuring and understanding strengths of planetesimal targets against disruption by impacts. Earlier experiments on which we based our estimates of "impact strengths" (e.g., Hartmann, Icarus 33, 50) were based on impacts into semi-infinite targets, in which only the projectile fragmented. The new experiments involved collisions with various mass ratios, where both target and projectile broke. These experiments tested the hypothesis applied in our numerical simulations: The energy is partitioned half into the target and half into the projectile, regardless of the target/projectile mass ratio. In Figure 3, the mass ratio of largest fragment to initial mass is plotted against the energy density delivered to the object under this hypothesis. It can be seen that for a wide range of conditions (projectile mass/target mass =

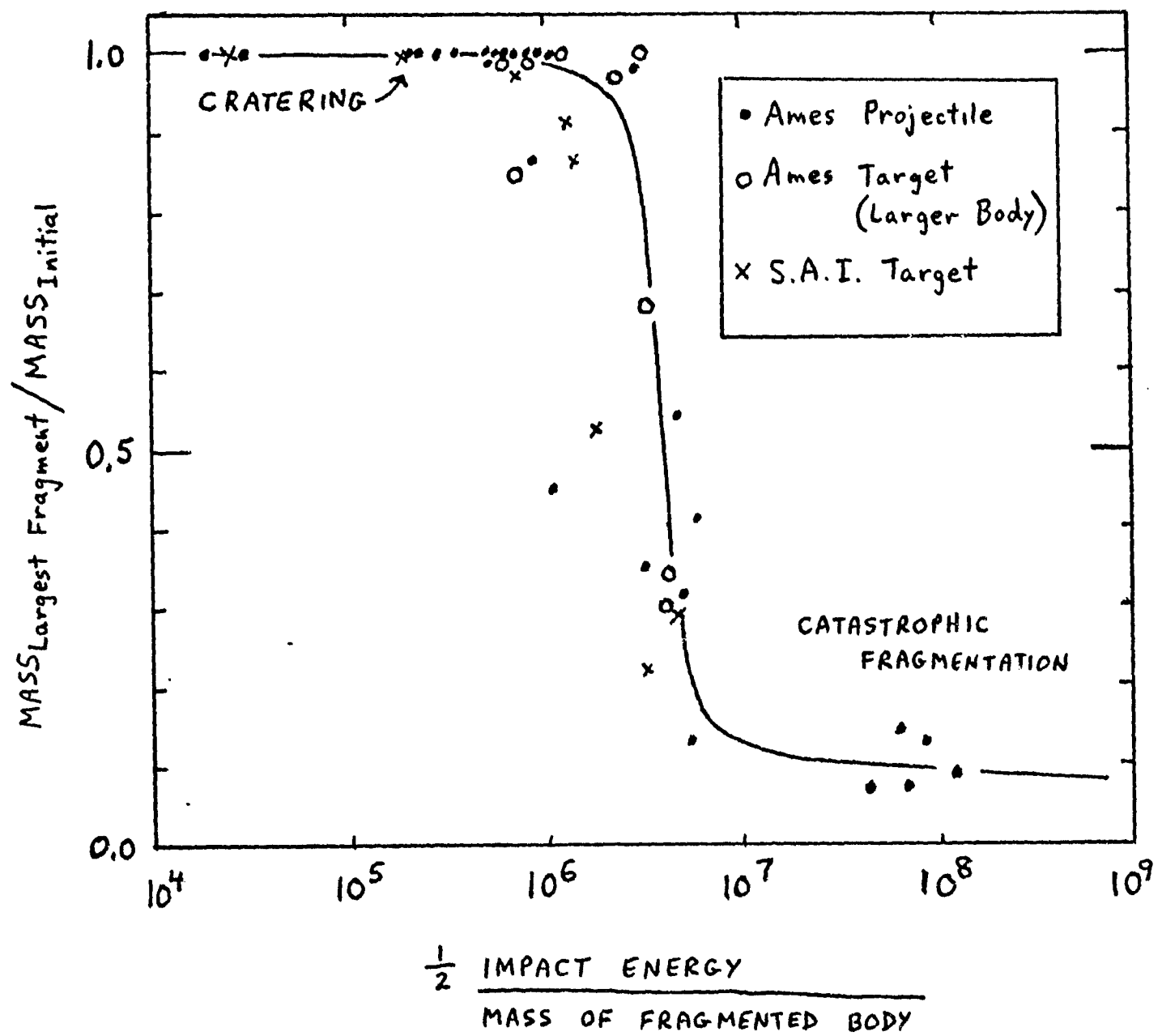


FIG. 3

0 to 1; velocity = 10 to 150 m/s; data for projectile and data for target), a rather well-defined curve divides the cratering regime from the regime of "catastrophic fragmentation" (the case in which the largest fragment \leq half the mass of the original. The limiting energy density is rather well-defined near 3×10^6 ergs/g in these new data. This implies an "impact strength" of $\sim 10^7$ erg/cm³. Since both the targets and projectiles follow the same curve, we conclude that our hypothesis of 1/2 of the energy being delivered to each is reasonable. This impact strength is about half of that found in previous interpretations of experimental data where all the energy was assumed delivered to the target.

S.A.I. Santa Ana Facility

A program of impact experiments was initiated during the past year in cooperation with the SAI impact laboratory in Santa Ana, California. The experiments performed to date were part of a no-cost precursor program to see if this facility was suitable for carrying out experiments relevant to problems of planet formation. The experiments carried out are summarized in Table 1. Targets were fine grained, irregular shaped basalts showing evidence of surface weathering collected on Sentinel Peak near Tucson. Sample No. 4 had several a priori hairline fractures, but the others appeared

TABLE 1: SUMMARY OF SANTA ANA IMPACT EXPERIMENTS

Target No.	Impact Speed (m/s)	Projectile Mass (gm)	Impact Energy (ergs)	Target Mass (gm)	Mass Largest Fragment (gm)	Impact Mass (cgs)	Impact Energy/Target Mass (cgs)	Final Mass Ratio/Initial
3	236	18.66	5.20 ⁹	3425.5	3330		1.5 ⁶	.97
11	126	18.53	1.47 ⁹	644.0	554.7		2.3 ⁶	.86
6*†	130	5.031	4.25 ⁸	918.0	909.7		4.6 ⁵	.99
6*†	52	4.855	6.56 ⁷	909.7	909.3		7.2 ⁴	1.00
6*†	303	4.790	2.20 ⁹	909.3	820		2.4 ⁶	.90
10	140	4.872	4.77 ⁸	172.1	91.2		2.8 ⁶	.53
4	621	5.585	1.08 ¹⁰	3106.9	693.3		3.5 ⁶	.22
8	238	4.760	1.35 ⁹	295.9	82.5		4.6 ⁶	.28

* Mass of largest post impact fragment

† Target #6 was hit three times

Note: Exponent notation means, e.g., $5.20^9 \equiv 5.20 \times 10^9$

unfractured.

Our results are plotted on Figure 3 for comparison with our Ames experiments. Note that the "impact strength" appears to be about a factor of 2 less than for the Ames experiments. This may be due to an intrinsic relative weakness in the field material. Based on the measured impact strength, these basalts would fall between the "intermediate material" and "solid rock" cases of Greenberg et al. (1978, Icarus 35, 1). Alternatively, it is conceivable that the glass projectiles deliver more than half the impact energy to the basalt targets. This will be tested by repeating similar experiments with basalt projectiles. Such results on the dependence of collision outcomes on material properties may have important implications for solar system evolution.

Other aspects of the collisional model of Greenberg et al. may be compared with these experimental results. For example, outcomes from our Santa Ana "cratering" experiments (i.e., those in which only a small portion of target material was removed) can be compared with the results predicted by our numerical algorithm. For solid rock, the mass of ejecta is computed by "energy scaling" with a scaling coefficient, $K = 10^{-9}$ gm/erg. However, we find that this predicts much smaller amounts of ejecta than the experiment yielded (Table 2).

TABLE 2: PREDICTED VS. EXPERIMENTAL TOTAL EJECTA MASS

TARGET ROCK	PREDICTED EJECTA MASS ($K = 10^{-9}$ cgs)	EXPERIMENTAL RESULT
3	2.6 gm	95 gm
6 (first shot)	0.2 gm	8.3 gm
6 (second shot)	0.03 gm	0.4 gm
6 (final shot)	1.1 gm	99 gm

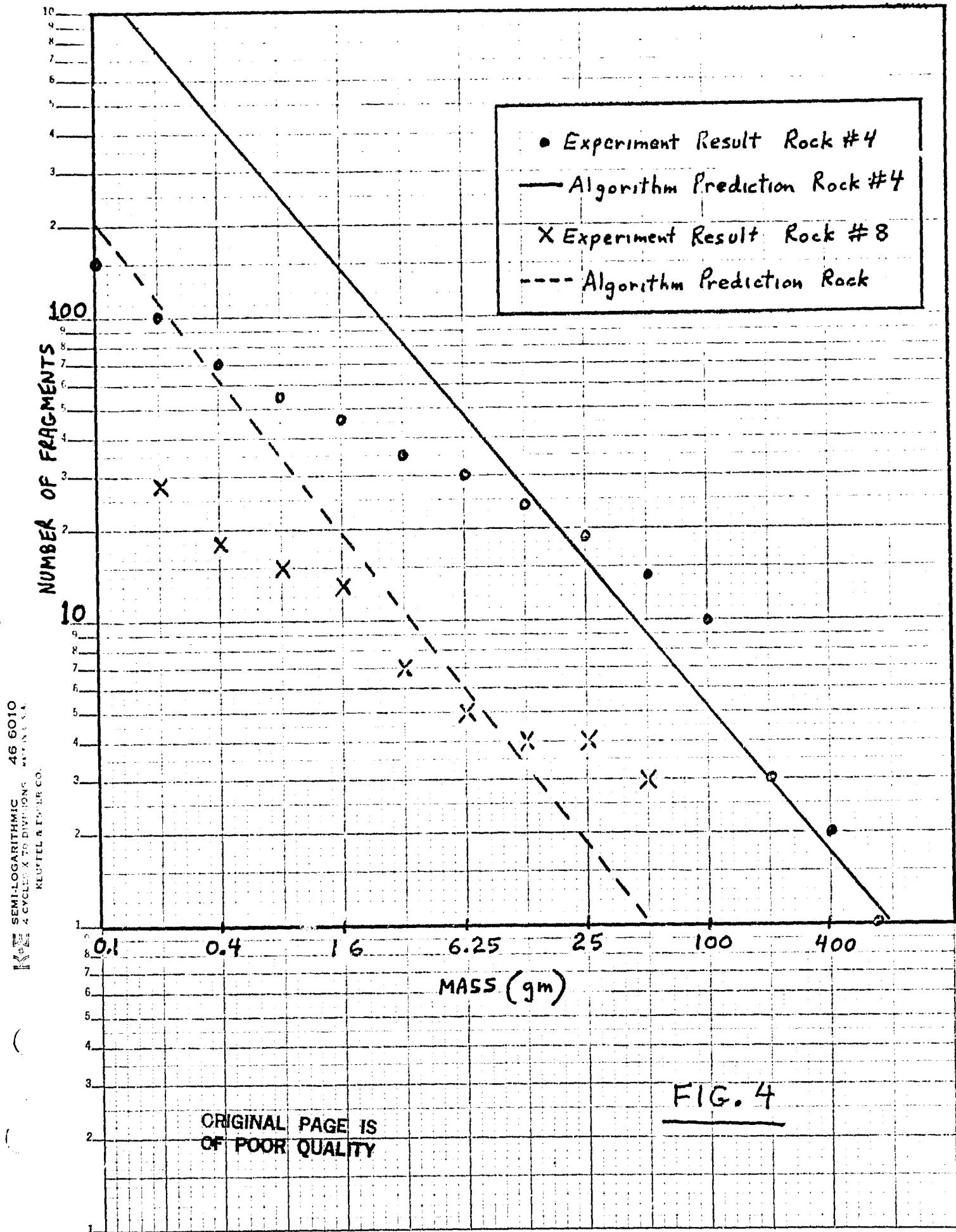
value $K \sim 4 \times 10^{-8}$ (greater than that for craters formed in sand) would be required to describe such results. "You do experiments and you learn things," a famous scientist has noted. In this case, the discrepancy between our experimental results and our numerical algorithm (which was based on a compilation of previous experimental data for cratering) is due to a qualitative difference between the damage inflicted by these experiments and the formation of craters. In this case, the damage is of a chipping and/or spalling nature. Moreover, the irregular shapes of the targets have protrusions (relative to a spherical shape) which are more prone to breaking off. For these reasons, the simple "cratering" algorithm is just not applicable.

We plan further experiments of this type in order to develop an algorithm to model these chipping events. At the same time, we need to consider both experimentally and by comparison with our knowledge of small-body properties, the conditions under which this algorithm should be applied. For example, asteroid observations show that irregular shapes are common over the km to ~ 100 km size range. Thus, the planetesimals in our numerical simulation perhaps would be treated more realistically with a "chipping" algorithm under certain conditions. The continuing work in this area illustrates how our numerical planet-growth simulation evolves in response to our

detailed technical studies of relevant processes.

Next we consider the size distribution of debris created in the examples of debris of catastrophic fragmentation (Target rocks #4 and #8). The size distribution predicted by the numerical algorithm are plotted for comparison with the experimental results. The impact strength inferred for these rocks from Figure 3 has been used to construct the predicted distribution. The predicted size of the largest fragment agrees well in each case with the experimental results. However, the remainder of the fragmental distribution is somewhat different from that predicted by the Greenberg et al. algorithm; in particular, the predicted slope is steeper than is actually observed, as is shown in Figure 4. Further analysis is needed, both to extend the data base and to understand the cause of the discrepancy.

The modeling of the large size end of the distribution may need to be re-examined. For example, Sample 8 produced three large fragments of approximately the same size rather than the predicted single object. The excess number of large objects mandates a lower slope in the



remainder of the distribution relative to that theoretically predicted. The other sample fragmented into a distribution that is better represented by two power law segments, with the large size portion having a steeper slope than the small size end. In both cases, the smaller size population is significantly overestimated by our theoretical algorithm. Similar "non-linearitics" in the size distribution of debris were found by Fujiwara et al (Icarus 31, 277, 1977).

The experimental program to date has provided useful results for validating our computational algorithms and pointing toward areas of deficiency in the models. The Santa Ana facility does appear suitable for carrying out further experiments there this year using their holographic imaging system to record the mass-velocity distribution of ejecta from high-speed impacts.

APPENDIX B.3

HYDRODYNAMIC CODE COLLISION CALCULATIONS

HYDRODYNAMIC CODE COLLISION CALCULATIONS

Large computer codes developed to carry out hydrodynamic flow calculations have been applied to study hypervelocity impact cratering by J.B. Bryan, D.E. Burton, M.E. Cunningham and L.A. Lettis, Jr. (PLSC 9, 1978, p. 3931-3964), J.D. O'Keefe and T. J. Ahrens (Science 198, 1249-1251, 1977; PLSC 7, 3007-3025, 1976), and R. Bjork (JGR 66, 3379-3387, 1961), and other groups. We initiated a pilot project during the past year to try to extend hydrodynamic calculations to the case of catastrophic disruption of finite targets by high speed impacts. Our second objective was to obtain a capability of predicting outcomes for certain of our experimental shots and comparing the observed and predicted results.

In cooperation with SAI's Huntsville office, a two-dimensional Eulerian finite difference code, HULL, was applied to investigate two problems. Computer time and labor to carry out these calculations were contributed by SAI. The first case treated was a simulation of the Meteor Crater impact event for comparison with published solution of Bryan et al. (1978), using the initial conditions of Bryan et al. The comparison is still underway (the donated effort is done on a time available basis). However, readily available parameters calculated by HULL are in good agreement with the published solution. For example, Figure 1 compared projectile

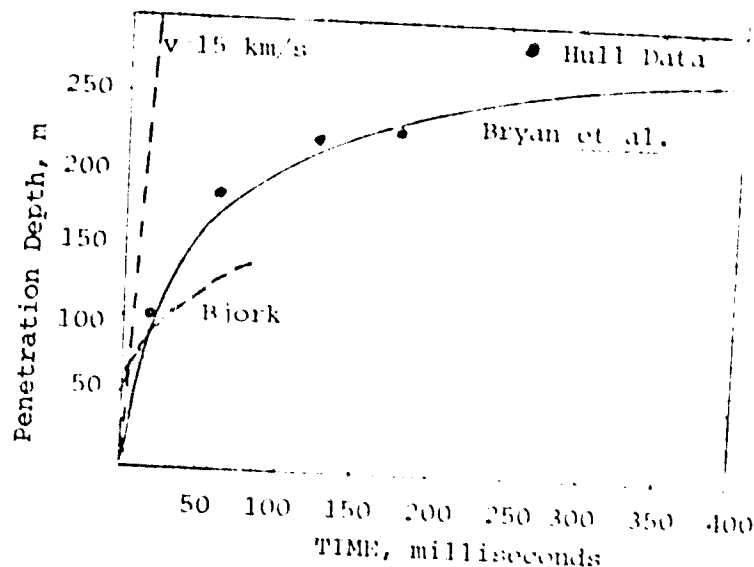


FIGURE 1

penetration depth as a function of time from HULL with the solution of Bryan et al.

The second case investigated with HULL was a simulation of two 1 km radius granite spheres colliding at 1 km/sec. Figure 2 shows a cross-section of the impacting bodies at several intervals based on HULL output. The calculation, such as velocity distribution of ejecta, will be carefully evaluated to see if they are plausible. Fragment sizes based on this calculation must be treated with caution for material strength failure is the only fragmentation mechanism considered in the model.

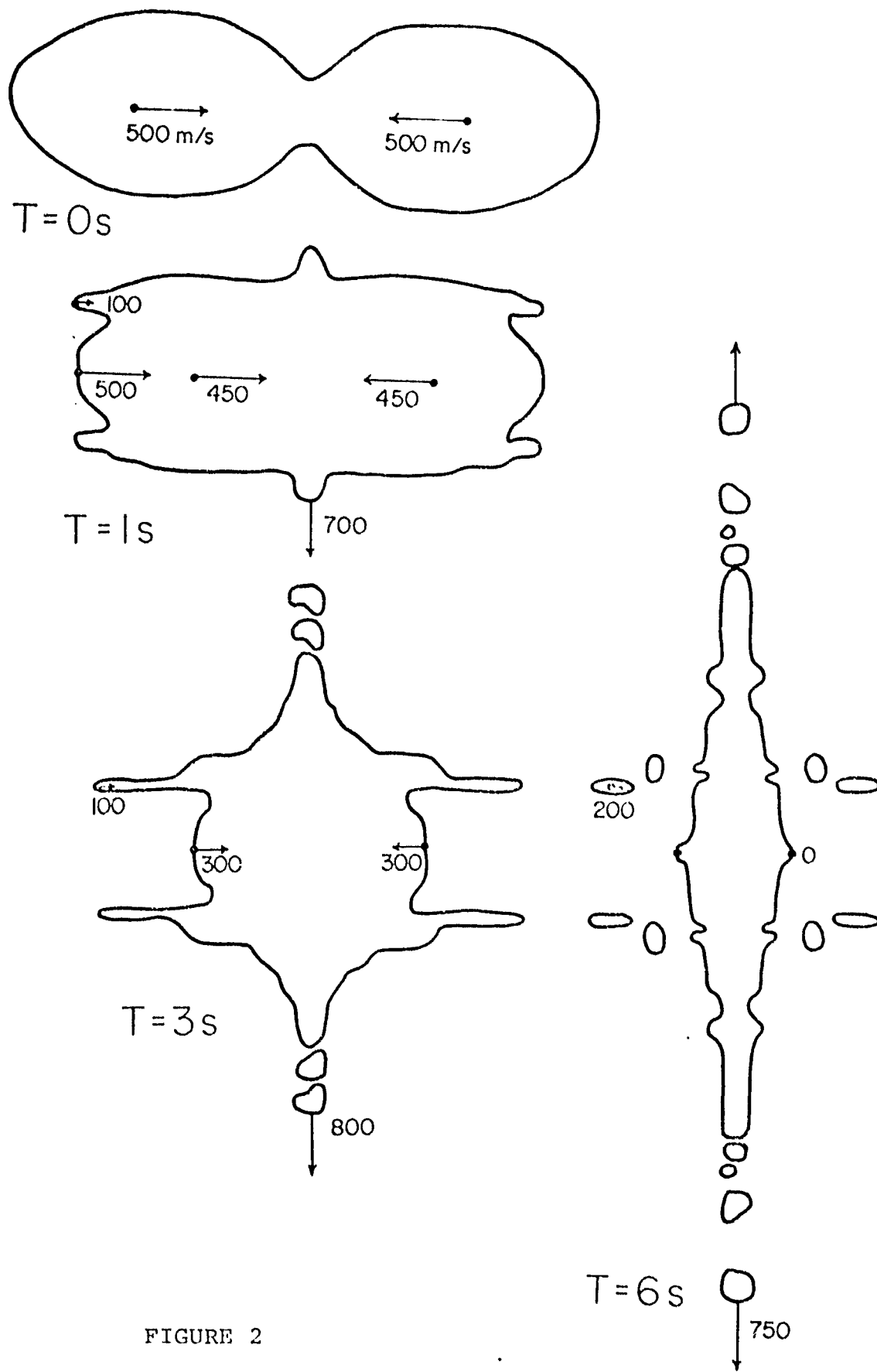


FIGURE 2

APPENDIX B.4

ORBITAL ELEMENT CHANGES DUE TO
GRAVITATIONAL SCATTERING

ORBITAL ELEMENT CHANGES DUE TO GRAVITATIONAL SCATTERINGIntroduction

Collisional velocities play a fundamental role in determining the evolution of a planetesimal swarm. If velocities become too large, collisional destruction and erosion results and the distribution proceeds to grind itself down, as is happening today in the asteroid belt. On the other hand, low encounter speeds result in accretion and growth of larger bodies. Collision speeds between particles are altered by interaction with other particles in the distribution - increased due to gravitational scattering and decreased by collisional damping. The model for velocity changes due to gravitational scattering previously in the program was developed for initial stages of planetesimal growth as described by Greenberg *et al.*, (1978). We are now extending and improving our model for velocity changes due to close encounters of bodies, in particular with application to scattering by intermediate- and large-sized (10^2 - 10^4 km diameter) bodies.

The basic problem is to find changes in mean orbit elements due to a large number of random gravitational encounters between n_1 bodies, each of mass m_1 , moving on orbits uniformly distributed within increments Δa , Δe and Δi centered on a_1 , e_1 and i_1 and a second population n_2 described by another set of parameters.

The other orbit elements - node longitude, periape longitude and mean anomaly are assumed to be uniformly distributed thru 360° . The patched or sequential conic model is adopted to simulate what are really three body interactions.

In this model, m_1 and m_2 are assumed to move on unperturbed conic orbits about the Sun when their mutual separation distance exceeds a critical distance. Within the critical separation distance, they move on conic orbits about their mutual mass center. The critical distance is referred to on the sphere of influence (SOI) which depends on the masses of the bodies and their distance from the Sun. The most common criteria for the size of the SOI, the Tisserand criterion, leads to a SOI radius

$$r_s \approx a \left(\frac{m}{M_\odot} \right)^{0.4} .$$

Comparison of results from patched conic models and fully integrated orbits (see Figs. 00 and 0) indicate generally rather good agreement except for distant, very low relative velocity encounters. By ignoring perturbations outside the sphere of influence, the patched conic model underestimates the frequency of small changes in orbital elements. The effect of a close gravitational interaction between two particles primarily produces a change in the heliocentric velocity vector of one or both particles. In the patched

conic model, the scattering process produces a rotation of the relative encounter velocity vector \bar{U} but does not change its magnitude. It is this rotation that changes the heliocentric velocity vector. Provided the encounter time is small compared with the orbital period and the SOI is small compared with the orbit, the position vector is essentially unchanged during the encounter. Hence the post-encounter (scattered) velocity vector can be transformed to equivalent orbit elements a , e , and i . By averaging over all possible encounter orbits, the mean value of the scattered velocity vector may be found which can then be expressed in terms of mean scattered orbit elements.

In the following sections we describe work in progress on two complementary methods of calculating changes in mean orbital elements due to close gravitational encounters based on the patched conic model. The first method (a) derives the probability distribution of orbit elements of the scattered body based on the mean deflection which is calculated with an approach analogous to that used by Wetherill (1967, JGR 72, 2429) in calculating orbital collision probabilities. The second method (b) is to statistically average over all possible encounter orbits using the deflection angle probability distribution of Weidenschilling (1975, AJ, 80, 145-153) and a uniform probability distribution of relative inclination angles. These two methods are used to determine the mean scattered heliocentric velocity vector from which the mean elements may

be found. Last year, reviewers of our proposal complained that we had not used enough equations to communicate our ideas. In this report a mathematical approach is appropriate and equations will be used liberally!

Method (a):

One approach to the problem is to extend the method developed by Wetherill (1976, JGR) for computing collision probabilities to the computation of probabilities of orbital element changes. First, we review Wetherill's method using a slightly different, but equivalent, mathematical approach that will be readily extendable to the velocity distribution problem.

How much of the time are two different orbits of given a , e , and i within a distance r of one another? The "field particle" elements will always be denoted by subscript 0. The orbital elements Ω , ω , $\Omega\omega$, and ω_0 (defined in Fig. 1) are assumed to vary uniformly with time so there is an equal probability of their having any value.



Fig. 1: Definition of Ω , ω .

Assume that the closest approach of the two orbits is in the vicinity of one of their mutual nodes. The position of a mutual node is given knowing $\Delta\Omega = \Omega - \Omega_0$ and i and i_0 . This geometry is shown in Figure 2.

FIGURE 00: Eccentricity distribution resulting after scatter from initially circular orbit distribution based on patched conic model.

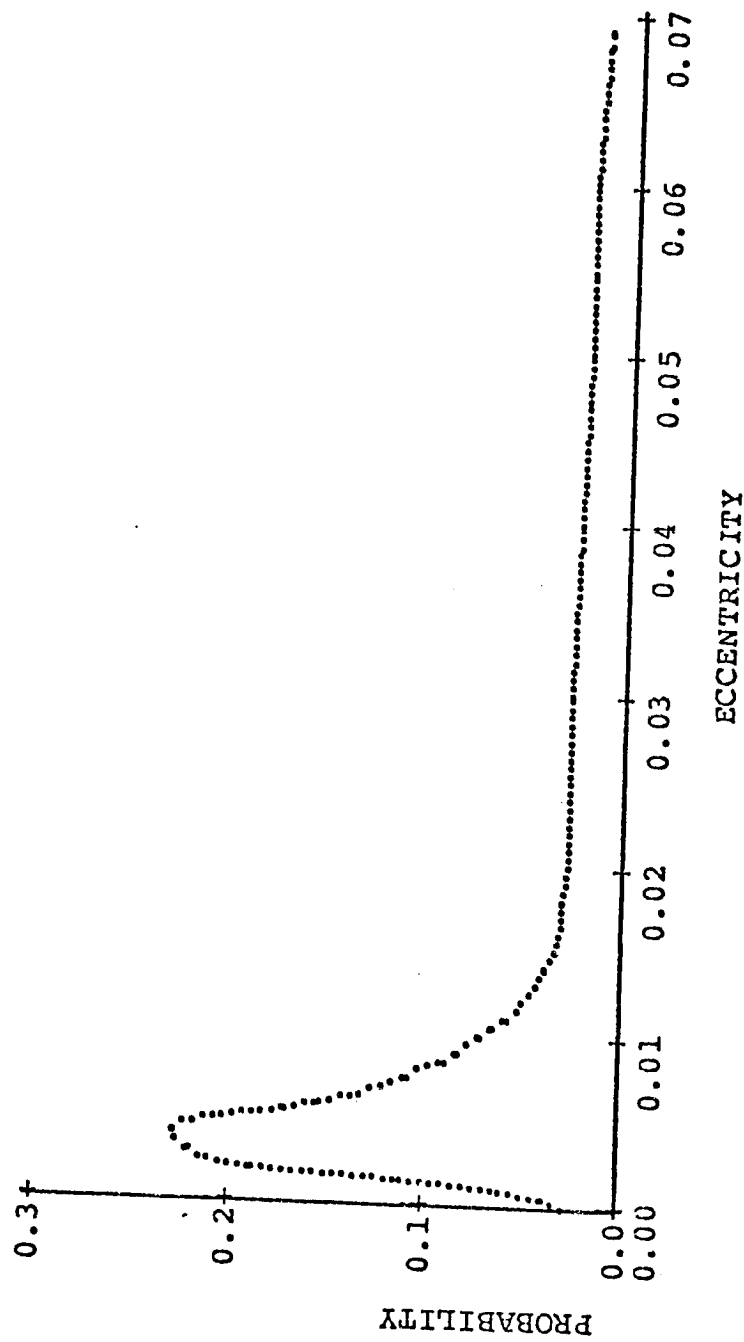
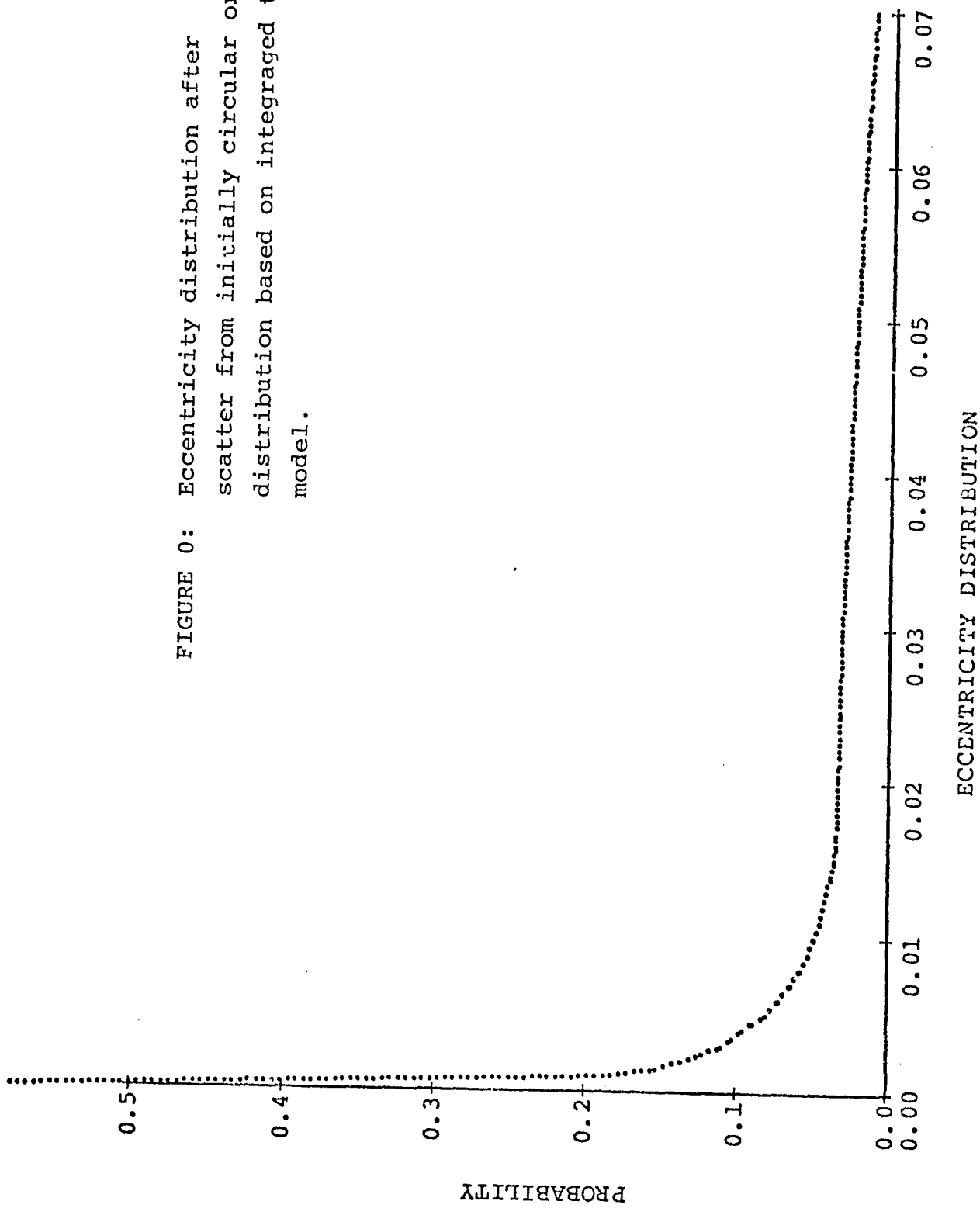


FIGURE 0: Eccentricity distribution after scatter from initially circular orbit distribution based on integrated trajectory model.



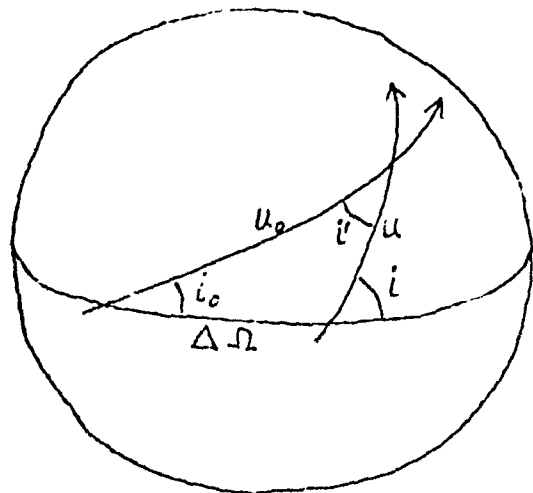


Fig. 2. Orbits projected on celestial sphere

Note that u_0 , u and i' are well-defined functions of i , i_0 and $\Delta\Omega$:

$$\cos i' = \cos i \cos i_0 = \sin i \sin i_0 \cos \Delta\Omega \quad (0 < i' < 180^\circ)$$

$$u_0 = \arctan \left[\sin \Delta\Omega / (\cot i \sin i_0 - \cos \Delta\Omega \cos i_0) \right] \quad (2 \text{ values, } 180^\circ \text{ apart})$$

$$\begin{aligned} \cos u &= \cos u_0 \cos \Delta\Omega - \sin u_0 \sin \Delta\Omega \cos i_0 \\ \sin u &= \sin u_0 \sin i_0 / \sin i \end{aligned} \quad \left. \begin{aligned} &\text{unique value, given } u_0 \\ &\text{selection} \end{aligned} \right\}$$

Consider a coordinate system with origin where field orbit crosses line of mutual nodes, with X directed outward along line of nodes and XY plane in the plane of the field particle's orbit:

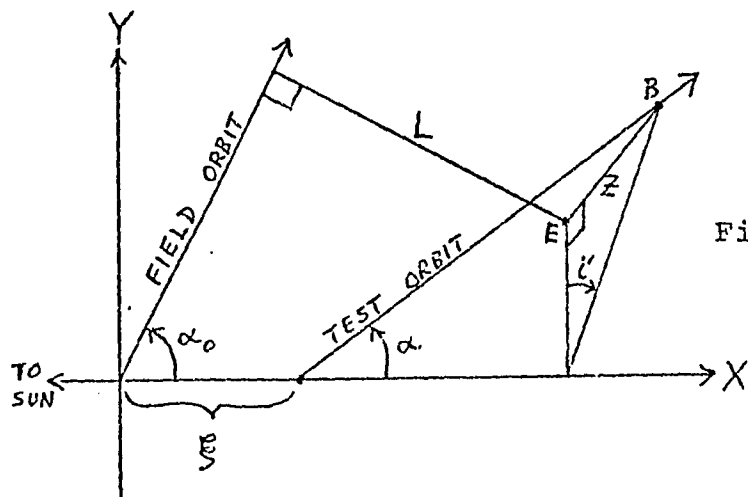


Fig. 3. Pt. $B(X, Y, Z)$ is on test orbit. Pt. E is its projection on XY plane.

Note α_0 is the angle the field orbit makes with the node line and α is the angle the test orbit makes with the node line. For a Keplerian orbit

$$\cot \alpha = \frac{e \sqrt{1 - \cos^2(u - \omega)}}{1 + e \cos(u - \omega)}$$

with a similar expression for α_0 . Also

$$\xi = \frac{a(1-e^2)}{1+e \cos(u-\omega)} - \frac{a_0(1-e_0^2)}{1+e_0 \cos(u_0-\omega_0)} .$$

The distance from any point B to the nearest point on the test orbit (assuming constant velocity, i.e., linear trajectories, near the mutual node) is $d = \sqrt{L^2 + Z^2}$ where

$$L = (X - Z \cot \alpha_0 \cot i') \sin \alpha_0$$

$$Z = (X - \xi) \tan \alpha \sin i'$$

Setting $d(d^2)/dX = 0$ we find the value of X (i.e., the particular position on the test orbit) which minimizes $|d|$:

$$X = \xi \frac{ts^2 - tcc(1-tcc) \sin^2 \alpha_0}{(1-tcc)^2 \sin^2 \alpha_0 + ts^2}$$

$$\text{where } ts \equiv \tan \alpha \sin i'$$

$$tcc \equiv \tan \alpha \cot \alpha_0 \cos i'$$

With this X,

$$L = \frac{ts^2 \sin \alpha_0}{(1-tcc)^2 \sin^2 \alpha_0 + ts^2}$$

$$Z = \frac{(tcc-1) \sin^2 \alpha_0 ts}{(1-tcc)^2 \sin^2 \alpha_0 + ts^2}$$

Hence,

$$d_{\min}^2 = \xi^2 \frac{ts^2 \sin^2 \alpha_0}{ts^2 + (1-ts^2)^2 \sin^2 \alpha_0}$$

or, in a form more symmetrical in terms of field and test particle

$$d_{\min}^2 = \frac{\xi^2 \sin^2 i'}{\cot^2 \alpha + \cot^2 \alpha_0 + \sin^2 i' - 2 \cot \alpha_0 \cot \alpha \cos i'}$$

If d_{\min} is less than τ , the collision cross-section radius of the two bodies, the orbits pass close enough to one another that collision is possible. What can we say about the $d_{\min}=0$ surface in $(\omega, \omega_0, \Omega, \Omega_0)$ space? First note that the geometry is independent of the absolute values of Ω and Ω_0 and only really depends on $\Delta\Omega$. So we want the $d_{\min}=0$ surface in $(\omega, \omega_0, \Delta\Omega)$ space. Setting aside the special case $\sin i'=0$, $d_{\min}=0$ only where $\xi=0$, i.e. where

$$\frac{a(1-e^2)}{a_0(1-e_0^2)} = \frac{1+e \cos(u-\omega)}{1+e_0 \cos(u_0-\omega_0)}$$

This defines a surface in $(\omega, \omega_0, \Delta\Omega)$ space.

Consider the cross-section of the $d_{\min}=0$ surface at $\Delta\Omega=0$. Note the linear relation between $\cos(u-\omega)$ and $\cos(u_0-\omega_0)$. The ambiguity in \arccos and in u and u_0 allows typically four values of ω (if any) for which $d_{\min}=0$, given

all the other orbital elements (cf. Wetherill's Fig. 1).

For any other $\Delta\Omega$, the $d_{\min}=0$ locus has the same size and shape, except that its position is shifted according to the values of u and u_o . We can consider an equivalent space $(\Delta\Omega, C, C_o)$ where

$$C \equiv \cos(u - \omega_r) \text{ and } C_o \equiv \cos(u_o - \omega_o).$$

For any given $\Delta\Omega$, $d_{\min}=0$ locus is a straight line

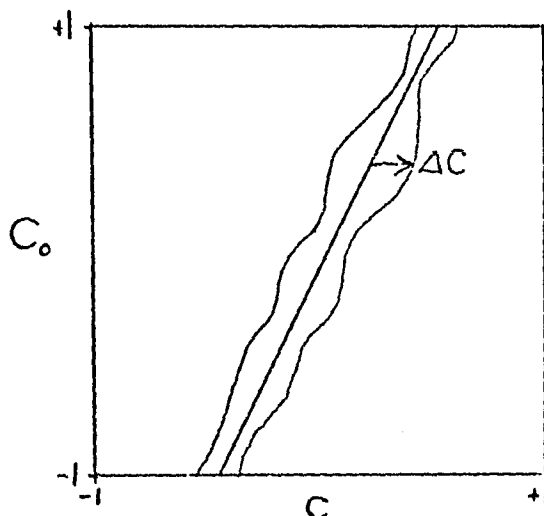


Fig. 4. $\Delta\Omega=\text{constant}$ plane has $d_{\min}=0$ as a straight line. $d_{\min} < r$ in a region defined by ΔC .

There is some region about the straight line ($d_{\min}=0$) in which $d_{\min} < r$. How big is this region? Consider

$$d_{\min} = \left[\frac{a(1-e^2)}{1+eC} - \frac{a_o(1-e_o^2)}{1+e_oC_o} \right] \left[\frac{\sin i'}{\sqrt{\cot^2 \alpha + \cot^2 \alpha_o + \sin^2 i' - 2 \cot \alpha \cot \alpha_o \cos i'}} \right]$$

Take

$$\left. \frac{\partial d_{\min}}{\partial C} \right|_{d_{\min}=0} = - \frac{a(1-e^2)e}{(1+eC)^2} \left[\frac{\sin i'}{\sqrt{\text{ditto}}} \right]$$

Then

$$\Delta C = r / \left(\left. \frac{\partial d_{\min}}{\partial C} \right|_{d_{\min}=0} \right)$$

$$\Delta C = \tau \left[- \frac{(1+eC)^2}{ae(1-e^2)} \right] \frac{\sqrt{V_{\text{ditter}}}}{\sin i'}$$

$$\text{where } \cot \alpha = \frac{e \sqrt{1-C^2}}{1+eC} \text{ and } \cot \alpha_0 = \frac{e_0 \sqrt{1-C_0^2}}{1+e_0 C_0}$$

$$\text{and } C = \left[(1+e_0 C_0) \frac{a(1-e^2)}{a_0(1-e_0^2)} - 1 \right] / e.$$

Therefore, ΔC is of form $\tau f(C_0)$. The differential area in which $d_{\min} < \tau$ is $2\tau f(C_0) dC_0$. The factor 2 accounts for both sides of the $d_{\min} = 0$ line. We really want the area in $(u-\omega, u_0-\omega_0)$ space, over which the a priori probability distribution is uniform:

$$\begin{aligned} 2 \Delta(u-\omega) d(u-\omega_0) &= 2 \left[\frac{d(u-\omega)}{dC} \Delta C \right] d(u_0-\omega_0) \\ &= 2 \left[\tau f(C_0) / \sin(u-\omega) \right] d(u_0-\omega_0). \end{aligned}$$

An additional factor of 2 is required for the ambiguity of 2 mutual nodes, so the area for which $d_{\min} < \tau$ is

$$\begin{aligned} &\int 4\tau f(C_0) (1-C^2)^{-1/2} d(u_0-\omega_0) \\ &= \int_{\omega_0}^{\infty} 4\tau f(C_0) (1-C^2)^{-1/2} d\omega_0 \end{aligned}$$

Such an integral, when extended over $d(\Delta\Omega)$ will give the volume in $(\omega, \omega_0, \Delta\Omega)$ space in which $d_{\min} < \tau$. However, that is not a sufficient condition for collision. We also need to compute, for a given $d_{\min} < \tau$, the probability of collision, i.e., the probability that both bodies will be near where their orbits come together at the same time.

Consider the coordinate system shown in Fig. 5 in which the z axis is defined by the direction of d_{\min} from the test to the field orbit and the y axis is parallel to the field body velocity \vec{U}_o . The velocities at closest approach are assumed to be the same as at the mutual node. \vec{U} lies in the xy plane. When the test body is at the

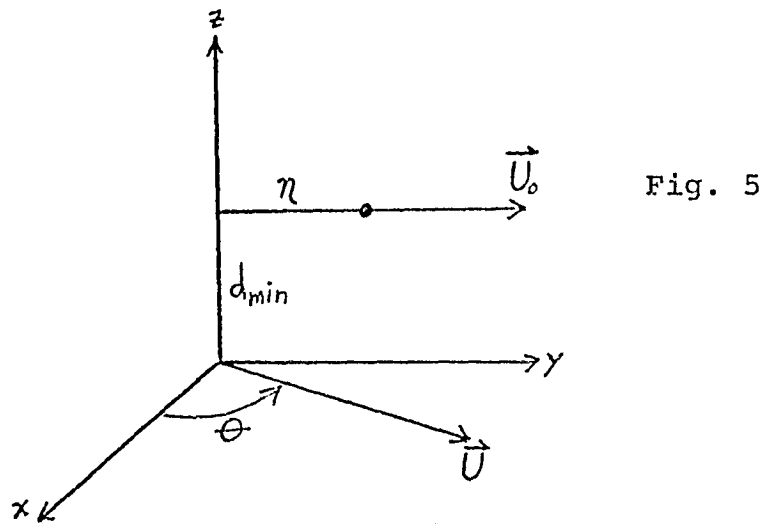


Fig. 5

origin, the field body is at $y=\eta$ ($t=0$). Separation of the two bodies is Δ :

$$\Delta^2 = (tU \cos \theta)^2 + (\eta + U_o t - Ut \sin \theta)^2 + d_{\min}^2$$

Taking $d(\Delta^2)/dt=0$ we find

$$\Delta_{\min}^2 = \eta^2 U^2 \cos^2 \theta / U_{\text{rel}}^2 + d_{\min}^2$$

when

$$t = \eta [U \sin \theta - U_o] / U_{\text{rel}}^2 \quad \text{where} \quad U_{\text{rel}} = |\vec{U} - \vec{U}_o|.$$

For a collision we require $\Delta_{\min} < \tau$:

$$\text{If } d_{\min} = 0, \text{ we require } n^2 \leq \frac{\tau^2 U_{\text{rel}}^2}{U_{\text{rel}}^2 \cos^2 \theta} \equiv n_1^2.$$

$$\text{If } d_{\min} = K\tau \text{ where } 0 < K < 1, \text{ we require } n^2 \leq n_1^2 (1 - K^2).$$

Thus the probability of collision for any given d_{\min} is $\sqrt{1 - K^2} \times$ probability if $d_{\min} = 0$. Therefore the average probability is

$$\int_0^1 \sqrt{1 - K^2} dK = \pi/4$$

times the probability if $d_{\min} = 0$.

Now, given that $d_{\min} = 0$, what is the collision probability?

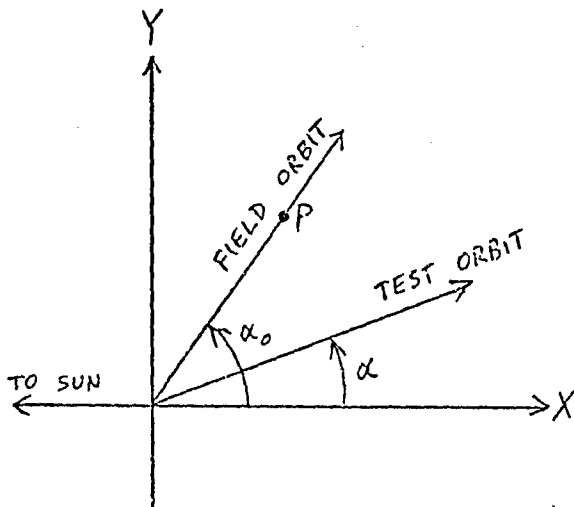


Fig. 6: Same as Fig. 1 except $d_{\min} = 0$. Field orbit is in XY plane; Test orbit is out of plane.

At $t=0$, test body is at point P with $(x, y, z) = (n \cos \alpha_0, n \sin \alpha_0, 0)$.

Wetherill shows that collision occurs if

$$|n| < \tau U_{\text{rel}} / [U_{\text{rel}}^2 - (U_{\text{rel}x} \cos \alpha_0 + U_{\text{rel}y} \sin \alpha_0)^2]^{1/2} \equiv n_0$$

\therefore Probability of collision each time test particle arrives

at origin is (time during which $\eta < \eta_0$)/(orbital period)

$$= \frac{2\eta_e}{U_e} \cdot \frac{1}{T_e}$$

From Keplerian theory we know U_e :

$$U_e^2 = \frac{GM(1 + e_e^2 + 2e_e \cos(\omega_e - \omega_i))}{a_e(1 - e_e^2)}$$

and also

$$T_e = \frac{2\pi a_e^{3/2}}{\sqrt{GM}}.$$

Probability of collision per time averaged over all $d_{\min} < \tau$:

$$\frac{\pi}{4} \frac{2\eta_e}{U_e} \frac{1}{T_e T}$$

The net probability is that expression times the fraction of total $(\omega, \omega_0, \Delta\Omega)$ space for which $d_{\min} < \tau$:

$$P = \frac{1}{\pi^3} \int_{\Delta\Omega \neq 0}^{\pi} \int_{\omega_e}^{\pi} 4\tau f(C_e) [1 - C^2]^{-1/2} \left(\frac{\pi}{4}\right) \frac{2\eta_e}{U_e} \frac{1}{T_e T} d\omega_e d\Delta\Omega.$$

This probability has been evaluated for several cases for comparison with Wetherill's result. In particular, the hypothetical asteroid "Astrid" ($a = 2.75$, $e = 0.2727$, $i = 0.2760$) has been considered in pair with various real bodies. The following table compared the results we obtain with those obtained by Wetherill (method equivalent to ours) and earlier by Arnold (simplified method). The probabilities are given for τ^2 :

TABLE: Comparison of three ways of computing probabilities of collision with "Astrid"

<u>Object</u>	<u>Arnold</u>	<u>Wetherill</u>	<u>Us</u>
1948 EA	1.92	3.10	2.49
Apollo	3.03	4.22	3.24
Adonis	4.95	4.13	3.92
1950 DA	2.19	3.90	3.13
Geographos	0	0	0
Icarus	0	0	0
Encke	2.56	3.49	2.91
Brorsen	0.79	0.94	0.81
Grigg-Mellish	0.020	0.022	0.021

Given that the method described above was supposed to be equivalent to Wetherill's, why do the numerical results differ? We can suggest a couple of explanations, although there may be other, more important ones that we haven't thought of yet. First, Wetherill's assumed (second column, p. 2434) that the collision probability for a given $\theta_0 \equiv u_0 - \omega_0$ can be integrated uniformly over θ_0 to get the average probability. In fact, some values of θ_0 may be more probable than others because of the eccentric motion. Second Wetherill used an averaging system in which he evaluated the probability at a number of randomly selected values of θ_0 and averaged them, rather than doing a numerical integration as we did. Whatever the reasons, our results agree to the level of precision required for Wetherill's 1967 conclusions. We should (and we intend to) be sure to understand the differences if we are to make

other applications of our theory, however.

In a gravitational interaction the relative velocity vector is rotated towards the direction of the minimum separation vector. The previous discussion includes evaluation of all the elements of the required geometry. The \vec{d}_{\min} can be expressed in a vector form pointing from the field to the test particle's orbit (in XYZ coords, see Fig. 3):

$$\vec{d}_{\min} = \begin{Bmatrix} L \sin \alpha_0 \\ L \cos \alpha_0 \\ Z \end{Bmatrix} = \begin{Bmatrix} g \frac{t_0^2 \sin^2 \alpha_0}{(1+t_0^2)^2 \sin^2 \alpha_0 + t_0^2} \\ g \frac{t_0^2 \sin \alpha_0 \cos \alpha_0}{\text{same denominator}} \\ g \frac{t_0 \sin^2 \alpha_0 (t_0 - 1)}{\text{same denom.}} \end{Bmatrix}$$

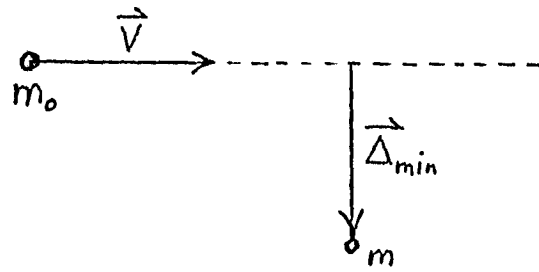
This vector is the line of minimum distance between the two orbits.

The vector of minimum separation is given by considering the values of η and of t at minimum separation as in the discussion of Fig. 5 and then rotating to the (X, Y, Z) system of Fig. 3:

$$\vec{d}_{\min} = \vec{d}_{\min} + \begin{Bmatrix} -(\eta + U_0 t) \cos \alpha_0 + Ut \cos \alpha \\ -(\eta + U_0 t) \sin \alpha_0 + Ut \sin \alpha \cos i' \\ Ut \sin \alpha \sin i' \end{Bmatrix}$$

where t was found earlier and θ (in the expression for t) comes from α, α_0 , and i' by spherical trig.

Now the field particle's velocity relative to the test particle is $\vec{v} = \vec{U}_0 - \vec{U}$.



B.4.17

Fig. 7

This relative velocity is rotated by angle 2χ where

$$\sin \chi = \left(1 + \frac{\Delta_{\min}^2 V^4}{G^2 (m + m_0)^2} \right)^{-1/2}$$

$$\text{so } \Delta \vec{U}_0 = \frac{m}{m_0 + m} V \sin 2\chi \hat{\Delta}_{\min} \\ - \frac{m}{m_0 + m} V (1 - \cos 2\chi) \hat{V},$$

a well-defined solution in terms of given orbital elements.

Let the components of $\Delta \vec{U}_0$ in (x, y, z) be $(\delta_1, \delta_2, \delta_3)$. These are the same components of ΔV used by Danby (1962) in his equations for the orbital element changes which correspond to a given ΔV . So, we get

$$\Delta \Omega_0 = \frac{\sqrt{1 - e_0^2} \sin u_0 \cos i_0}{n_0 a_0 (1 + e_0 \cos(u_0 - \omega_0))} \delta_3$$

and similar changes for Δe_0 , Δi_0 , etc. Thus for any given 2 sets of orbital elements we have the change in elements at closest approach near the nodes. Note that these equations work only if closest approach is near the nodes. Therefore we must set all changes equal to 0, if Δ_{\min} is greater than some critical value such as the "sphere of influence". Also require that ea , ia , $e_0 a_0$, $i_0 a_0 \gg$ that critical distance.

Conclusion: We can obtain the probability distribution for orbital element changes by computing all changes over uniformly space ω , ω_0 , $\Delta\Omega$ and mean anomaly of the field particle when the test particle is at the point of d_{\min} . By taking the average in this way, all changes will be "per orbital period of test particle".

In calculating the changes in orbital elements, we really should consider both nodes. However, except in special cases, only 0 or 1 of them will have an interaction within the sphere of influence.

Note: One thing we should have shown earlier is how η is related to the mean anomaly M_0 of field particle when test particle is at d_{\min} point:

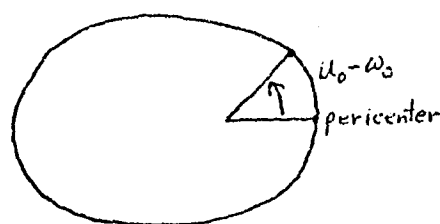


FIGURE 7:

We know that the mean anomaly at the mutual node is given by the usual relation between mean anomaly and true anomaly, $u_0 - \omega_0$:

$$m_{\text{node}} = f(u_0 - \omega_0)$$

which you get from Kepler's equation.

Then a time $(M_0 - M_{\text{node}})/n_0$ later is when the field particle is at its d_{\min} point. At that time the field particle is a distance $U_0 (M_0 - M_{\text{node}})/n_0$ past the node. Thus

$$\eta = U_0 (M_0 - M_{node})/n_0 - Q$$

where Q is the distance from the node to the d_{\min} point on the field particle's orbit.

What is Q ? Refer to Fig. 3:

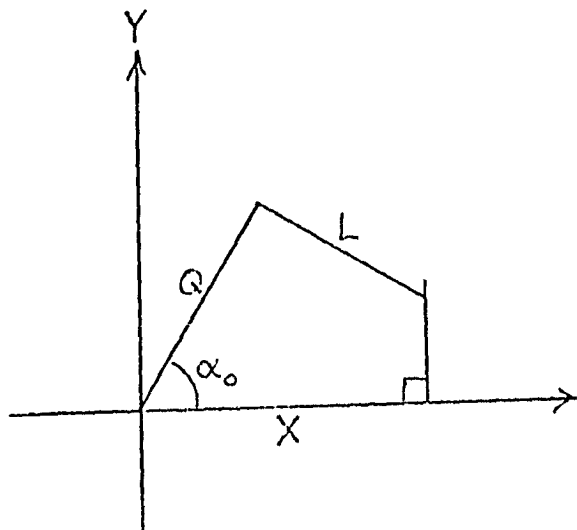


FIGURE 8:

$$Q \cos \alpha_0 + L \sin \alpha_0 = X$$

$$Q = \frac{X - L \sin \alpha_0}{\cos \alpha_0}$$

where X and L have been evaluated previously.

Method (b) :

An alternative approach makes use of probability distributions for the rotation angle of the relative velocity vector and for the plane of the relative encounter trajectory. In the following analysis we use the equivalent single body scattering model.

For simplicity, assume $m_2 \gg m_1$ so that the center of mass is at m_2 (when the masses are comparable, the relative orbits can always be expressed as equivalent one body orbits). At any position on the scattering body (m_2) orbit where close approaches between m_1 and m_2 are possible, we assume that there will be sufficient numbers of particles that statistical averaging is meaningful, but few enough so that there are seldom three or more bodies within the SOI at once.

Consider a particular position on the orbit of m_2 specified by its heliocentric distance, r_2 . Encounters are possible with the fraction of m_1 particles having periapses oriented such that the heliocentric distance to m_1 at the relative node of the orbits is nearly equal r_2 . The heliocentric velocity components and relative velocity vector can be found from relations given by Ópik (1976, Interplanetary Encounters). For a particular pair m_1 and m_2 , the patched conic model required transforming the orbit of m_1 from heliocentric to mass centered when m_1 is at the sphere of influence of m_2 .

The approach conditions of m_1 , relative position and velocity at the sphere of influence, define a hyperbolic encounter trajectory of m_1 about m_2 . When m_1 is again at the sphere of influence on the outward leg of the trajectory, the orbit is "patched" back into a heliocentric conic orbit, which generally is different from the pre-encounter heliocentric orbit of m_1 . The effect of the close encounter is dominantly to change the heliocentric velocity vector of m_1 via a rotation of the relative velocity vector during the encounter. The angle through which the relative velocity vector rotates, ν , depends on the impact parameter, b , relative speed, U , and the mass of the scattering body, m_2 , and is

$$\tan \frac{\nu}{2} = \frac{G m_2}{b U^2} . \quad (1)$$

For any orientation of the orbit planes producing an intersection of the orbits, the relative speed is fixed. Hence, the post encounter heliocentric velocity is determined by the deflection angle ν and the plane in which the rotation occurs, which is the plane of the encounter hyperbolic trajectory relative to the scattering body, e_r . The mean value of the post encounter velocity vector may be found by averaging over all deflection angles and relative inclinations

assuming a uniform areal distribution of impact parameters.

The normalized probability distribution of deflection angles given the encounter speed U is given by Weidenschilling (1975, AJ 80, 145-153).

$$P(v|U) dv = \frac{\cos(v_{12}) dv}{K \sin^3(v_{12})} \quad (2)$$

$$\text{and } K = \sin^{-2}\left(\frac{v_{\min}}{2}\right) - \sin^{-2}\left(\frac{v_{\max}}{2}\right),$$

where v_{\max} and v_{\min} are deflection angles corresponding to trajectories that just graze the surface of the scattering body and to trajectories that just enter the sphere of influence, respectively. The initial relative velocity vector expressed in a coordinate system with x radially outward from the Sun, y being orthogonal to x in the orbit plane of the scattering body and z being perpendicular to the scattering bodies' orbit plane is given by (see Figure 9):

$$U_{x_0} = U \left(\cos \Omega_0 \cos \beta_0 - \sin \Omega_0 \sin \beta_0 \cos \iota_r \right)$$

$$U_{y_0} = U \left(\sin \Omega_0 \cos \beta_0 + \cos \Omega_0 \sin \beta_0 \cos \iota_r \right) \quad (3)$$

$$U_{z_0} = U \sin \iota_r \sin \beta_0$$

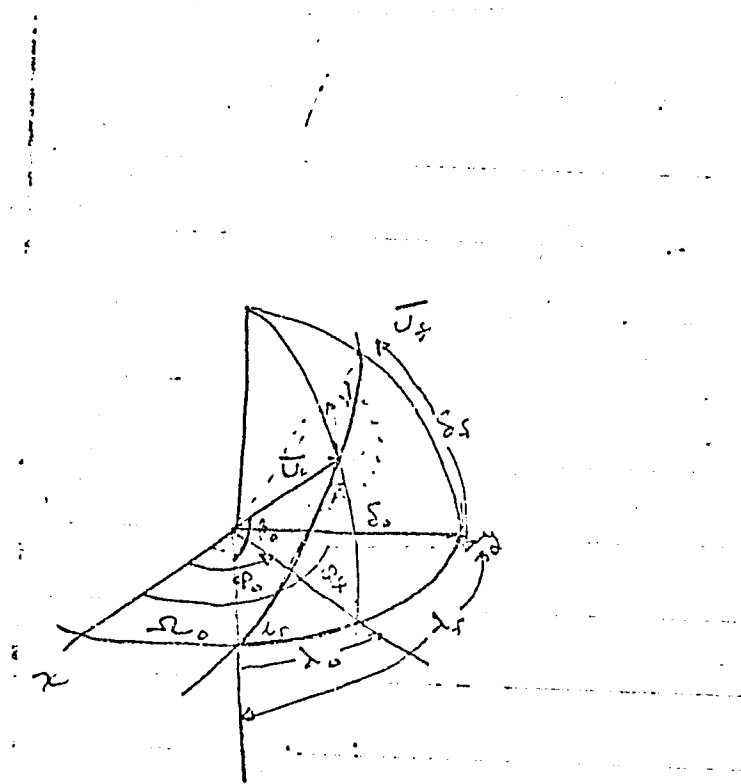


FIGURE 9: Geometry for rotation of relative velocity vector during gravitational scatter

During an encounter in a fixed relative orbit plane, the velocity vector is rotated to a final orientation given by $\beta_f = \beta_o + v$, hence the deflected relative velocity vector is found by replacing β_o with β_f in (3). Then mean values are found from

$$\bar{U}_x = \int_{\lambda_r} \int_v U_x(v, U, \lambda_r) P(v|U) P(\lambda_r) dv d\lambda_r$$

$$\bar{U}_y = \int_{\lambda_r} \int_v U_y(v, U, \lambda_r) P(v|U) P(\lambda_r) dv d\lambda_r$$

$$\bar{U}_z = \int_{\lambda_r} \int_v U_z(v, U, \lambda_r) P(v|U) P(\lambda_r) dv d\lambda_r$$

The final expressions are

$$\bar{U}_x = U_{x0} F_1(m_2, U) + 4C \tan S_o F_2(m_2, U)$$

$$\bar{U}_y = U_{y0} F_1(m_2, U) + 4C \tan S_o F_2(m_2, U)$$

$$\bar{U}_z = U_{z0} F_1(m_2, U)$$

where $F_1(m_2, U)$ and $F_2(m_2, U)$ depend only on the ratio

$\frac{U}{V_e}$, where V_e is the two body escape speed from m_2 , \tan

$S_o = \frac{U_{z0}}{\sqrt{\frac{U_{x0}^2}{2} + \frac{U_{y0}^2}{2}}}$ and C is a parameter depending only on

S_o and is of order unity.

To complete the averaging, we must average over all positions in the scattering bodies' orbit and over all orientations of the relative node of the two orbits. Prior to carrying out these calculations, however, we shall numerically evaluate the initial averaged equations to determine the variations expected in further averaging. The averaged equations for the scattered velocity components were evaluated for several scattering body masses, initial orbits and orbit orientation and these results are summarized in Table 2. As can be seen from this table, the variation in mean scattered elements with position around the orbit is not large and for most cases, the evaluation at quadrature provides a good approximation to the true mean when averaging over all positions in the orbit. Of major importance, however, is the variation with relative node, $\Delta\Omega$. The encounter velocity is determined partially by the relative inclination which, for a given pair of orbital inclinations, is determined by $\Delta\Omega$. The mean values of orbit velocity resulting from large numbers of randomly oriented individual encounters between bodies on given orbits is then found by averaging over all relative node orientations of the two bodies.

These expressions for the mean scattered orbit elements are being used to improve the velocity perturbation model in

the numerical simulation. During a timestep, the number of encounters between the n_1 particles moving on orbit 1 and n_2 particles moving on orbit 2 is calculated based on the particle-in-a-box model along with the new values of orbital elements of these particles that are scattered. Those scattered into new orbit element bins are removed from the old bins and added to the new ones, while those that aren't deflected completely out of the old bins are accounted for by recomputing the mean value of orbit elements for the particles currently in the bin. By repeating this procedure for each pair of mass and orbit element bin, the evolution of the orbit element distribution during the time step is found and a sequence of timesteps gives the evolution of the mean orbit element and hence the mean impact speed distribution. The present version of the numerical model treats a single planetary zone so the semimajor axis is a constant and only variations in the eccentricity and inclination of planetesimals are modeled. The linking of different planetary zones, necessary to model the simultaneous evolution and growth of planets, (see Section II) may ultimately require a detailed treatment of the semimajor axis evolution.

TABLE 2: EFFECT OF POSITION IN ORBIT AND RELATIVE ORIENTATION
ON MEAN DEFLECTION.

	a (AU)	e	i (deg)
Scattering Orbit	1.000	.010	0.0
Initial Scattered Orbit	1.000	.050	5.0
Final orbit when scattering position:			
Periapse	.999	.058	4.94
Quadrature	.998	.059	4.93
Apoapse	.999	.059	4.94
Scattering Orbit	1.00	.05	4.9
Initial Scattered Orbit	1.00	.05	5.0
Final orbit when			
(A) $\Delta\Omega = 0$			
Periapse	0.85	.12	5.2
Quadrature	0.84	.20	5.3
Apoapse	0.85	.23	5.3
(B) $\Delta\Omega = 90$			
Periapse	1.01	.06	11.8
Quadrature	1.01	.05	11.8
Apoapse	1.01	.04	11.8
(C) $\Delta\Omega = 180$			
Periapse	1.03	.08	14.5
Quadrature	1.03	.06	14.5
Apoapse	1.02	.05	14.5

APPENDIX B.5

VALIDATION OF MASS-SHIFTING ALGORITHM

VALIDATION OF MASS-SHIFTING ALGORITHM

The large number of bodies (typically 10^{12}) involved in simulations of planet growth clearly makes it impossible to follow the mass evolution of individual objects. The usual approach in such problems is to treat the mass distribution as a continuum, and set up a generalized integro-differential coagulation equation for its time variation (G.V. Pechernikova, V.S. Safronov, and E.V. Zvyagina, Sov. Astron., 20, 346, 1976). However, the numerical solution of such equations requires very large amounts of computer time, even when the coagulation probability can be expressed as a simple function of the masses only. Our use of realistic mechanical properties with a variety of collision outcomes, coupled with the simultaneous velocity evolution, makes this approach intractable. Instead, we use an approximate technique which conserves mass, but does not precisely account for numbers of particles. The basic method, described briefly by Greenberg et al. (1978), will be reported here in greater detail, followed by a description of work in progress to test and improve its accuracy.

(1) The mass distribution is divided into discrete size bins (usually spanning by a factor of two in mass). Interactions between bins (collisions and gravitational stirring) are computed as if all particles in a bin have the mean mass of that bin.

(2) During a time step, the number of bodies removed from a bin by accretion or catastrophic disruption in interactions with all other bins, and with itself, are calculated from particle-in-a-box statistics. The total net gain or loss of mass of the remaining bodies due to accretion or erosion is computed, and used to calculate the change in the mean mass in that bin.

(3) Suppose that at the beginning of a timestep, the total mass M in a bin is known. We have

$$M = N \bar{m}$$

where N is the number of particles in the bin, and \bar{m} is the mean mass. The change in mass during a timestep is

$$dM = Nd\bar{m} + \bar{m}dN.$$

The first term is evaluated in a straightforward manner, since the change in \bar{m} has been computed. In the second term, the change in the number of bodies, dN , has two components. One is due to those directly removed when accreted by other bodies or fragmented in catastrophic collisions. The other accounts for bodies which are assumed to lie near the boundaries of the bin, and can be "pushed" into another bin by a small change in mass.

We assume that the number of particles in a bin is distributed uniformly in $\log M$:

$dN/d \log m = C = \text{constant across the bin.}$

This gives $N = \int_{m_1}^{m_2} \frac{dN}{d \log m} d \log m = C \log (m_2/m_1)$,

where m_1, m_2 = lower and upper mass boundaries of the bin (Figure 1).

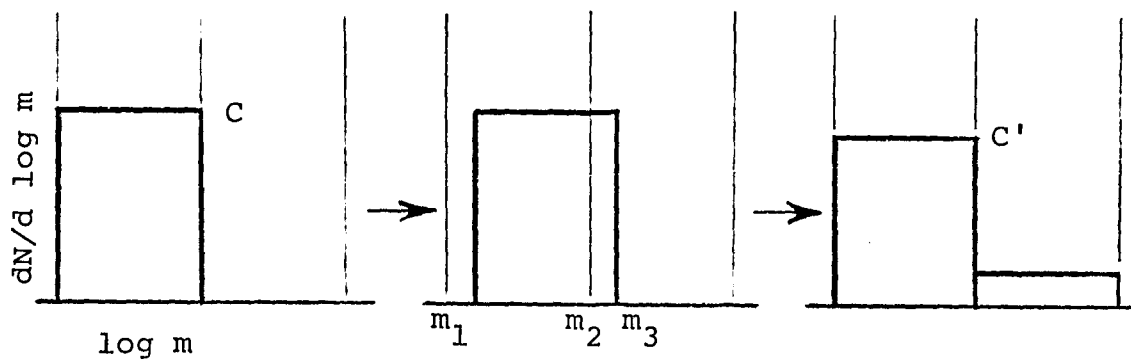
Then $m = \int m dN(m) = C(m_2 - m_1)$ and

$$\bar{m} = M/N = (m_2 - m_1)/\log (m_2/m_1).$$

Suppose, for example, that the mean change in mass per particle due to accretion and erosion in one timestep is Δm . For simplicity, we assume that each particle in the bin had its mass multiplied by the factor $(1 + \Delta m/\bar{m})$; this gives a uniform shift in $\log m$ across the bin. The mass is now uniformly distributed between $m_1(1 + \Delta m/\bar{m})$ and $m_3 = m_2(1 + \Delta m/\bar{m})$ (Figure 2). The mass pushed into the next bin is

$$\Delta M = \int_{m_2}^{m_3} m dN(m) = C(m_3 - m_2) = Cm_2 \Delta m/\bar{m}.$$

This mass is subtracted from the first bin and added to the next. The remaining mass in the first bin is no longer uniformly distributed, and must be adjusted before the next timestep. After all mass changes have been computed, so the total mass in a bin is M' , the number of particles is reset to $N' = M'/\bar{m}$, and in the next timestep, we use the value $C' = N'/\log (m_2/m_1)$.



Schematic of mass transfer algorithm. For clarity, only one bin is shown initially occupied.

FIGURE 1

Since this algorithm is only approximate, its degree of accuracy is of some concern. An exact solution is not required, but we certainly want our results to give a qualitatively correct picture of planet growth within our initial assumptions, and hopefully to produce quantitative results within an order of magnitude of "exact" solutions. We are cautiously optimistic that this is indeed the case, for the following reasons:

Analytical calculations using computed velocities and collision rates show that it is physically possible for the largest bodies to grow in the times elapsed; they do not appear to be artifacts of the program.

We find that for the growth of the largest bodies, the first term in the expression for dM ($N\bar{dm}$) dominates. This term, due to accretion of smaller bodies, does not depend on the mass shifting algorithm.

The program has been tested with a range of bin widths and timesteps, with little effect on the results.

We have tried variations in the mass-transfer algorithm. For example, C has also been computed from the average number of particles in adjacent bins, to approximate a continuous distribution. All versions tested to date give qualitatively similar results. The time to produce a largest body of a given size typically varies by about a factor of two.

The program logic has been applied to some simple coagulation problems for which analytic and numerical solutions exist (Scott, 1968). In tested cases, it has computed mass distributions which are generally well within an order of magnitude of the exact solutions, provided the mean mass of the distribution has not evolved by more than an order of magnitude. This condition holds in all planet-growth simulations run to date. Additional tests are planned, and we are experimenting with other mass-transfer algorithms in hopes of further improvement.

In extending our simulations to produce objects of planetary size, we can avoid further dependence on such approximations. Once the largest bodies become sufficiently few in number, they can be detached from the size distribution and treated as individuals, rather than as part of a bin population. This "hybrid" approach will be incorporated into the program during the current year.

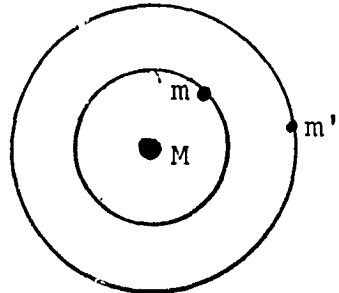
APPENDIX B.6

INCLINATION-TYPE RESONANCE
IN A DISSIPATIVE MEDIUM

INCLINATION-TYPE RESONANCE IN A DISSIPATIVE MEDIUM

Earlier work on orbital resonances in dissipative media (Greenberg, 1978) led to exciting new results relevant to planet-building and to the structure of rings and of the asteroid belt. Past work focused on eccentricity-type resonances, the simplest to treat mathematically. Now we are looking at inclination resonances, which are generally more difficult to treat because the relevant equations are non-linear. We next describe current progress in treating this problem: The governing equations have been solved analytically. We plan in the immediate future to use this new solution as a basis for including a dissipative medium in the analysis.

Consider perturbation of an interior satellite by a more massive perturber near the 2:1 resonance. Assume $m \ll m' \ll M$ and $i' = e = e' = 0$. The resonance variable (critical argument of the disturbing function) is



$$\psi = 4\lambda' - 2\lambda - 2\Omega$$

(The following analysis may not require the assumption that $i' = e' = e = 0$, as long as conditions are such that there are no other important resonance variables nearby. See Greenberg, MNRAS 165, 1973.)

The disturbing function takes the following form after eliminating short-period terms and higher order terms in i :

$$R = \frac{Gm' F i^2 \cos \psi}{a'} - \frac{1}{2} \frac{Gm'}{a'} i^2 \alpha b_{3/2}^{(+1)} - \frac{3}{4} \frac{GM}{a} J_2 (r/a)^2 i^2$$

where F and $b_{3/2}^{(+1)}$ are both functions of $\alpha \equiv a/a'$. See Greenberg (MNRAS 165, 1973) for details. Note $F \approx 0.2$ and $b_{3/2}^{(+1)} \approx 5$. Changing notation:

$$R = F_1 Gm' (i^2/a) \cos \psi - F_2 Gm' (i^2/a^2) - \frac{3}{4} GM (J_2 r^2/a^2) (i^2/a)$$

$$\text{where } F_1(\alpha) \approx 0.13$$

$$F_2(\alpha) \approx 1$$

Also let $F_1' \equiv \partial F_1 / \partial a$ and $F_2' \equiv \partial F_2 / \partial a$.

Now

$$\dot{\psi} = 4n' - 2n - 2\dot{\varepsilon} - 2\dot{\Omega}$$

where dots are time derivatives, ε is mean longitude at epoch, and other elements are standard notation. Evaluate rhs using standard perturbation equations:

$$\begin{aligned} \dot{\varepsilon} &= - \frac{2na^2}{GM} \frac{\partial R}{\partial a} + \frac{na}{GM} \frac{i}{2} \frac{\partial R}{\partial i} \\ &= - \frac{2na^2}{GM} \left[F_1' Gm' (i^2/a) \cos \psi - F_1 Gm' (i^2/a^2) \cos \psi \right. \\ &\quad \left. - F_2' Gm' (i^2/a) + F_2 Gm' (i^2/a^2) \right. \\ &\quad \left. + \frac{9}{4} GM J_2 R^2 i^2 / a^4 \right] \\ &+ \frac{na}{GM} \frac{i}{2} \left[2F_1 Gm' \left(\frac{i}{a} \right) \cos \psi - 2F_2 Gm' \left(\frac{i}{a} \right) - \frac{3}{2} \frac{GM J_2 R^2}{a^2} \left(\frac{i}{a} \right) \right] \end{aligned}$$

$$\dot{\varepsilon} = -2 \left(\frac{m'}{M} \right) (F_1' a - F_1) n i^2 \cos \psi$$

$$+ 2 \left(\frac{m'}{M} \right) (F_2' a - F_2) n i^2$$

$$- \frac{9}{2} J_2 (R^2/a^2) n i^2$$

$$+ \left(\frac{m'}{M} \right) F_1 n i^2 \cos \psi$$

$$- \left(\frac{m'}{M} \right) F_2 n i^2$$

$$- \frac{3}{4} (J_2 R^2/a^2) n i^2$$

$$\dot{\Omega} = \frac{na}{GMI} \frac{\partial R}{\partial i}$$

$$= 2 \left(\frac{m'}{M} \right) F_1 n \cos \psi - 2 \left(\frac{m'}{M} \right) F_2 n - \frac{3}{2} (J_2 R^2/a^2) n$$

Assume $\dot{\Omega} \gg \dot{\varepsilon}$ because $\dot{\varepsilon} \propto i^2$.

$$\psi = 4n' - \left[2 - 4 \left(\frac{m'}{M} \right) F_2 - 3 (J_2 R^2/a^2) \right] n - 4 \left(\frac{m'}{M} \right) F_1 n \cos \psi$$

Also evaluate \dot{n} and \dot{i} :

$$\dot{n} = -3 \frac{n^2 a}{GM} \frac{\partial R}{\partial \lambda}$$

$$\boxed{\dot{n} = -6F_1(m'/M)i^2n^2 \sin \psi}$$

$$\dot{i} = -\frac{na}{GMi} \frac{\partial R}{\partial \Omega}$$

$$\boxed{\dot{i} = -2 \left(\frac{m'}{M}\right) F_1 n i \sin \psi}$$

To simplify define

$$\left\{ \begin{array}{l} q = 4(m'/M) F_2 + 3(J_2 r^2/a^2) \\ dt = n' dt \\ n = n/n' \end{array} \right.$$

That yields

$$\left\{ \begin{array}{l} \frac{d\psi}{dt} = 4 - (2 - q) n - 4(m'/M) F_1 n \cos \psi \\ \frac{di}{dt} = -2(m'/M) F_1 n \cos \psi \\ \frac{dn}{dt} = -6(m'/M) F_1 n^2 \cos \psi \end{array} \right.$$

To simplify even further, assume that n as it appears in coefficients is nearly constant (n_0). That assumption is

generally valid in this type of analysis, but should be checked carefully before final acceptance of results (cf. Greenberg AJ 78, 1973). Next let

$$N \equiv 4 - (2 - q) n$$

$$I \equiv i^2$$

$$C \equiv -2F_1 n(m'/M)$$

Now the governing equations take the form:

$$\left\{ \begin{array}{l} \frac{d\psi}{d\tau} = N + 2C \cos \psi \\ \frac{dI}{d\tau} = 2CI \sin \psi \\ \frac{dN}{d\tau} = -3(2 - q) CIn_0 \sin \psi \end{array} \right.$$

Removing τ dependence:

$$\frac{dN}{dI} = -1.5(2-q)Cn_0 \Rightarrow \boxed{N - N_0 = -1.5(2 - q) Cn_0 (I - I_0)}$$

$$\frac{d\psi}{dI} = \frac{N_0 - 1.5(2 - q) Cn_0 (I - I_0)}{2CI \sin \psi} + \frac{1}{I} \frac{\cos \psi}{\sin \psi}$$

Let $\phi \equiv -I \cos \psi$

Then

$$\frac{d\phi}{dI} = I \sin \psi \frac{d\psi}{dI} - \cos \psi$$

$$\frac{d\phi}{dI} = \frac{N_0 - 1.5(2 - q) C n_0 (I - I_0)}{2C}$$

which yields

$$\phi = \frac{N_0 + 1.5(2 - q) C n_0 I_0}{2C} - \frac{3}{8} (2 - q) n_0 I^2 + \text{const}$$

where the constant is evaluated by setting $\phi = -I_0 \cos \psi_0$ and

$$I = I_0.$$

We thus have a solution for the trajectory in (n, i, ψ) space. This is a closed trajectory. In order to include dissipative effects, such as imposed changes in n due to gas drag or tides or in i due to drag, we intend in the immediate future to apply a variation of parameters approach such as that used by Greenberg (AJ 78, 1973).

Next consider the case in which $i' \neq 0$. In this case a resonance occurs where the resonance variable $\psi \equiv 4\lambda' - 2\lambda - \Omega - \Omega'$ is slow varying. Let us assume that precession of Ω and Ω' is such that this resonance is well separated from the one discussed earlier, i.e., that this ψ is the only slow-varying

argument. In this case, the equations of motion can be put in the form:

$$\left\{ \begin{array}{l} \frac{d\psi}{dt} = 4n' - 2n + (m'/M) n'(i'/i) F \cos \psi \\ \frac{di}{dt} = (m'/M) n'i'F \sin \psi \\ \frac{dn}{dt} = 6n (m'/M) ii'F \sin \psi \end{array} \right.$$

Since i' and F are nearly constant, these equations have the same form as the e -type resonance studied by Greenberg (Icarus 33, 1978), except that e is replaced by i . Hence, an i damping medium in this case will have the same effect as the e damping medium had in that case, namely a secular variation in semi-major axis. The effect will be somewhat weaker due to the extra small factor (i') which appears here. We intend in the immediate future to consider the implications of these results in solar system evolution. These are some examples of our continuing technical work on resonance effects in the early solar system.

APPENDIX B.7

THEORY OF ROTATIONS

THEORY OF ROTATIONS

Work was initiated on understanding and modeling the collisional evolution of planetesimal rotation in conjunction with the population size frequency evolution. The focus of this year's research was rotational evolution in collisional fragmentation models, particularly with application to asteroids. Analytic models for equilibrium rotation states of asteroids have been developed by Harris (Icarus in press 1979). The analytic rotation theory is applicable only to populations distributed according to a power law size-frequency distribution - a significant restriction in light of the plausible planetesimal, as well as observed asteroid, distributions. Large gravitationally bound asteroids are predicted to have rotation rates independent of size, but they rotate considerably slower than is predicted using our best estimates of collisional parameters combined with the Harris theory: 3 hours vs. the 9 hour observed mean rotation period. Hence, for the asteroid belt, either (i) our estimates of parameters are incorrect, (ii) collisional relaxation has not yet been reached in the present belt, or (iii) the restriction to power law populations precludes model results from being applicable to asteroids.

Option (i) is possible given that our knowledge of

impact physics at high speeds involving large bodies is quite limited. However, to reconcile theory and observation would require extreme values for some parameters, such as converting all the input collisional kinetic energy into ejecta kinetic energy. Option (ii) implies that there has been only a modest collisional evolution of asteroids, i.e., the asteroid belt was not substantially more massive initially than it is today. This result is consistent with results from collisional evolution modeling. Option (iii) is probably the most plausible, since the best determination of the asteroid size-frequency distribution indicates that the belt differs significantly from a power law distribution. Another shortcoming of the model is that the rotational models are applicable basically to a single generation population whereas most asteroids are multi-generation bodies, being fragments from collisions of larger bodies. The rotational distribution of a fragmental population probably is determined in part by the spin rates of the fragments from the catastrophic disruption of large bodies, whereas in the theory developed so far, it is assumed that fragments rotate at the same rate on the parent body. But, this is unrealistic since the kinetic energy that goes into rotation is influenced more by the total kinetic energy of the

collisions than by the pre-impact rotation speed of the parent body.

According to the model, for small bodies where material strength dominates over gravitational binding, the mean equilibrium rotation period is predicted to vary directly with the diameter of the asteroid - smaller bodies should rotate faster. Observations of asteroid rotations do suggest that small asteroids tend to rotate faster, although further observations are required to test the prediction of a linear dependence between rotation period and asteroid diameter.

Further work is planned for the current year on extending models of collisional rotation. Primarily, it is planned to treat numerically the simultaneous evolution of the size-frequency distribution and the rotation distribution. By treating the problem numerically, not only can the evolution of both distributions be followed, but also the restriction to power law distributions will no longer be required and arbitrary population distributions can be studied. The rotational evolution model will be applicable to the rotational distribution for accreting planetesimals and should be applicable to studying the rotational properties of the growing planets. Improved rotational models may permit us to distinguish whether or not the observed rotation periods of large asteroids are primordial or the product of collisions.

APPENDIX B.8

ORIGIN OF ASTEROIDS:
VELOCITY PUMPING BY LARGE
JUPITER-SCATTERED PLANETESIMALS

ORIGIN OF ASTEROIDS: VELOCITY PUMPING BY LARGE JUPITER-SCATTERED PLANETESIMALS

The present asteroid zone is unusual for its low mass density and high mean collision speed (~ 5 km/sec); neither condition could have existed at the time asteroids formed. With the present mass density, intervals longer than the age of the solar system would be required to accrete Ceres-sized bodies, while a mean collision speed of 5 km/sec produces collisional destruction rather than accretion for asteroidal size bodies. However, the low mass density may be a consequence of the high collision speed, because collisional grinding will produce an asteroid-like mass distribution on a timescale less than the age of the solar system as shown by the collisional evolution models of Davis et al. (1979), provided most of the mass is initially in bodies less than a few hundred km diameter. However, it has not been shown that velocity pumping preceded mass depletion. For example, the same process that increased collision speeds may have also caused a mass loss, or conceivably mass depletion could have occurred by a totally different process prior to velocity pumping. Jupiter is usually invoked as the agent for these effects.

Various investigators, e.g., Safronov (1972, NASA TT F-677) and Weidenschilling (1974, Icarus 22, 426-435) have argued

that impacts of Jupiter-scattered planetesimals (JSP) on early asteroids were responsible for the low mass density and high relative velocities. Alternatively, Heppenheimer (1979, LSC-X Abs. 531-533) and Ward (1978, B.A.A.S. 2, 591) have suggested that Jovian secular resonances swept through the inner solar system as nebular gas dissipated and augmented planetesimal eccentricities and inclinations. Presumably the asteroid zone was affected to some extent by this latter hypothesized mechanism because there are still secular resonances in the belt today. However, let us consider first the effects of JSP's. Davis et al. (1979, see Appendix A.4) argue that asteroids are too weak to have their velocities changed appreciably by collisions; they will be destroyed by large collisions before there are enough small impacts to significantly change their orbits. We suggested that gravitational stirring by large Jupiter-scattered planetesimals could have effectively pumped up asteroid velocities on a timescale comparable with the elimination of JSP by Jupiter. In this scenario, a growing proto-Jupiter was accompanied by a size distribution of other bodies in this zone, some of which were gravitationally deflected into the asteroid zone.

To test the JSP scattering hypothesis, we have carried out numerical simulations using a version of our planet forming program that was modified to simulate asteroid collisional evolution as part of a separately funded program to study asteroids. The velocity pumping model is a

preliminary version of the algorithm described in Appendix B.4. The increase in mean asteroid collision speed with time is shown in Figure 1 for the case of an earth-sized body in a Jupiter-crossing orbit, but having its perihelion deep within the asteroidal zone. In this case, gravitational stirring by the massive JSP increases the mean asteroid collision speed from 200 m/sec to 5 km/sec in $\sim 2 \times 10^7$ years; an interval comparable to the mean lifetime of bodies on Jupiter-crossing orbits. Subsequent collisional evolution among asteroids would reduce the initial asteroid population to the present observed population, provided that there were few additional original asteroid larger than 500 km diameter.

The advantages of this JSP scenario for the early evolution of asteroidal velocities are: (1) there is no problem in eliminating the JSP, since the same agent (Jupiter) that brings them into the asteroid belt also removes them from the belt. (2) The stirring is accomplished by gravitational encounters rather than by collisions. (3) Large asteroids, such as Pallas with its 35° inclined orbit, are stirred as effectively as small bodies. (4) The reduction of mass in the asteroidal zone may be accomplished either by collisions with an accompanying population of smaller JSP or by collisions among the asteroids at their enhanced velocities, depending on the original mass distributions of both population components. (5) The existence of one or

more Earth-sized JSP is a plausible accompaniment to the formation of the outer planets (although its necessity remains to be demonstrated) and the timescale for their evolution is reasonable.

Possible limitations of this scenario include: (1) There is no ready explanation of the Kirkwood gaps; they must be formed by a different process than the velocity pumping mechanism. (2) The degree of gravitational stirring depends on the random orbital evolution of the few largest Jupiter-scattered bodies, and therefore on the statistics of small numbers. More rigorous calculations are being planned to show that such an event, together with subsequent collisional evolution among the asteroids themselves, can produce the observed distributions of eccentricities and inclinations, as well as their mean values.

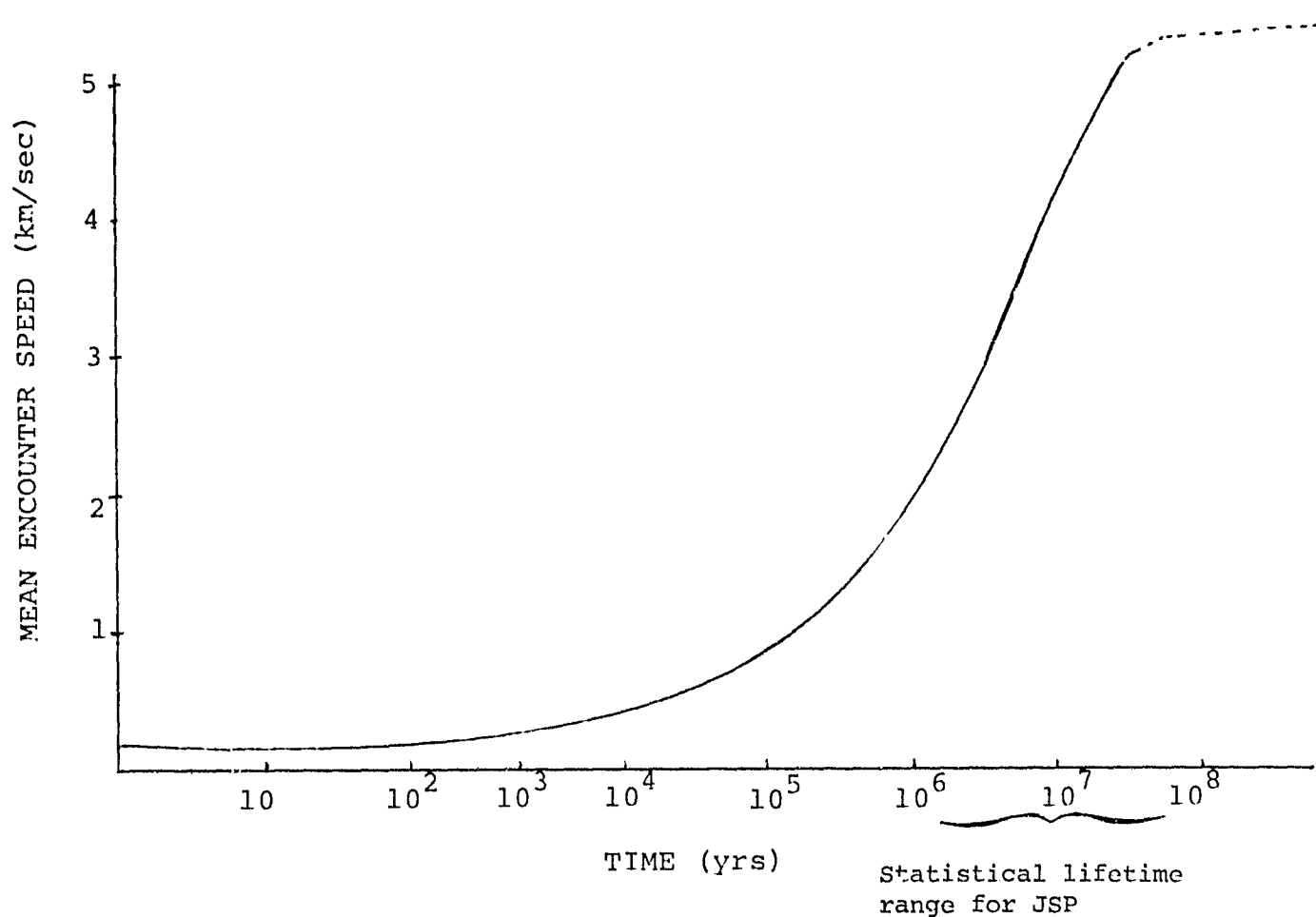


FIGURE 1

APPENDIX Q.1

"Formative Conditions Controlling Structure of Planetary Highlands." An Abstract submitted to the Lunar Highlands Conference by William K. Hartmann

FORMATIVE CONDITIONS CONTROLLING STRUCTURE OF
PLANETARY HIGHLANDS. William K. Hartmann, Planetary Science
Institute, Tucson, Arizona 85719.

Crater densities on highlands (or the most heavily cratered surfaces) of Moon, Mercury, Mars, Phobos, and Deimos reach remarkably similar values (Fig. 1), relative to the wide scatter of densities in other provinces. This coincidence may be telling us something about highland structure, and suggests some mechanism that defined an envelope of crater densities rarely exceeded on planetary landscapes. This process is likely to be a saturation or steady state mechanism, implying repeated pulverization of highlands, producing deep megaregoliths.

Reconstruction of early accretionary cratering (Fig. 2) can be done invoking (1) present-day observed flux rates; (2) observed decay of meteorite flux from 4 Gy ago to present, based on dated lunar samples; and (3) flux rate necessary to build Earth and Moon in time intervals compatible with meteorite formation intervals. The impact flux in the "missing" years from 4.5 to 4.0 Gy ago ranged about 10^3 to 10^7 times the present flux rate, had an average 20 to 45 my half-life, caused enormous rates of megaregolith production, and does not appear to require any anomalous "spike" of catastrophic cratering around 4.0 Gy ago.

Relative timing between magma ocean cooling, and decay rate of cratering was very important in controlling present day observed character of planetary highlands, since it controlled outcome of competition between preservation of intact igneous rock and conversion of igneous rocks into massive breccias.

HIGHLAND FORMATIVE CONDITIONS

Hartmann, W.K.

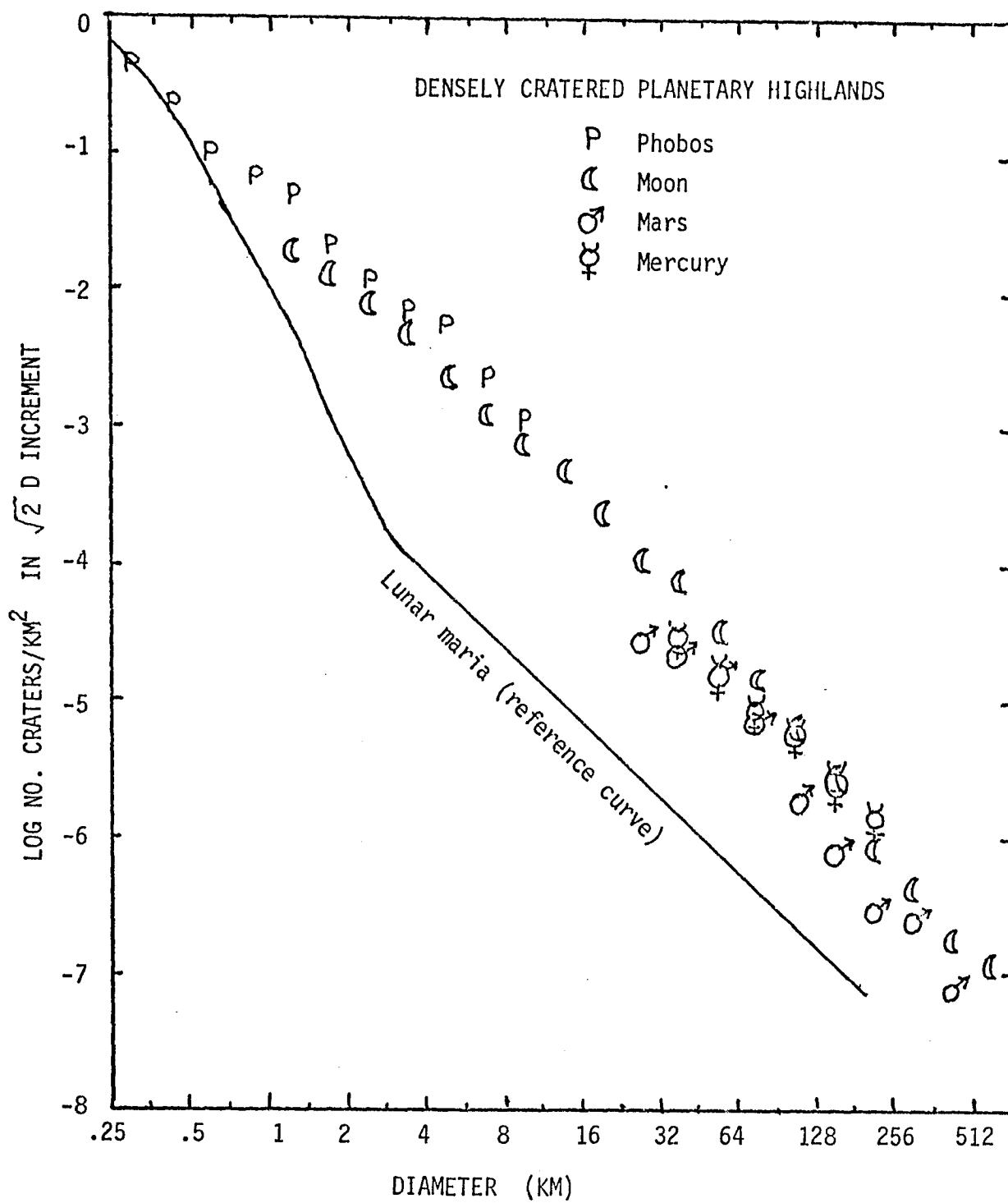


FIGURE 1. Crater densities on "highlands" provinces on several planets lie near values about $32 \times$ those found among large craters in lunar maria. Clustering is tight relative to diversity of values in other provinces.

Hartmann, W.K.

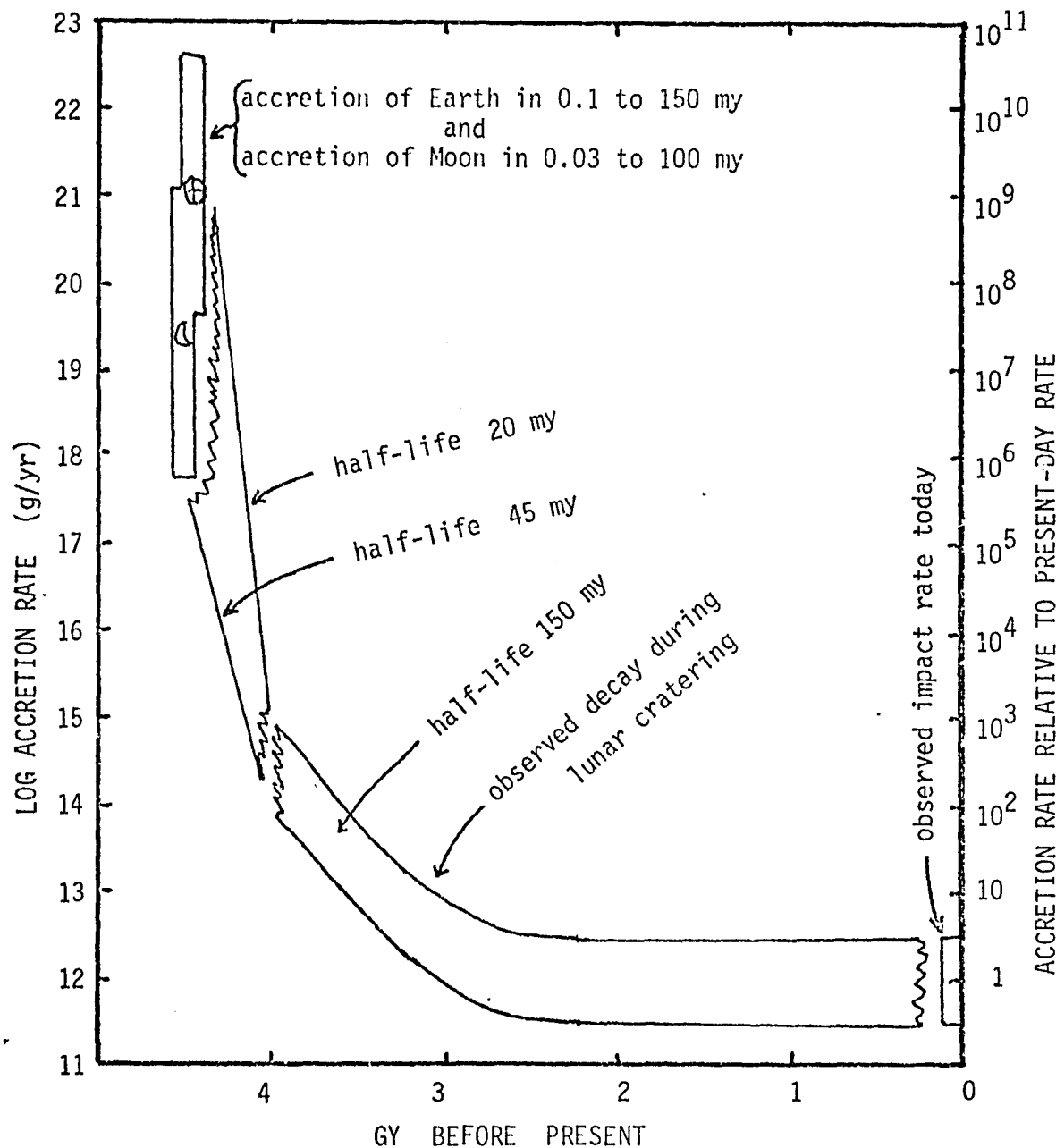


FIGURE 2. Schematic reconstruction of accretionary cratering without invoking a "spike" of catastrophic cratering 4 Gy ago. Present rate is observed (lower right) and projected back to 4 Gy ago using known impact rates determined from lunar dating. Additional datum is impact rate required to form Earth and Moon during their estimated formation intervals. Connection in "missing interval" from 4.5 to 4.0 Gy gives plausible planetesimal sweepup half-lives of the order 20 to 45 my.

APPENDIX Q.2

"Early Runaway Growth of Planets." An Abstract
submitted to the Division of Planetary Science
meeting of the American Astronomical Society
in St. Louis, 1979, by Richard Greenberg

Early Runaway Growth of Planets. RICHARD GREENBERG, Planetary Sci. Inst. (Tucson) - Extension of our numerical simulation of planet growth beyond the stage previously reported (Greenberg *et al.*, *Icarus*, 35, 1, 1978) indicates that the largest body in an accretion zone grows so much faster than smaller bodies that, by the time it is a few thousand km in diameter (only $\sim 5 \times 10^4$ yr after collisional accretion begins), it is detached from the continuous size distribution of planetesimals. As it becomes detached, but not before, it reaches a size such that a significant fraction of the zone's mass resides in the largest body. This scenario contradicts assumptions in analytical models of planet growth (Safronov, NASA TT F-677, 1972) that the largest bodies contain most of the mass throughout most of the growth period and that they all remain part of the continuous portion of the size distribution. We are searching for material and system parameters that might yield evolution consistent with Safronov's assumption. Our model does give relative velocities of planetesimals consistent with Safronov's analytical results: The velocities are on the order of the escape velocities of those bodies which dominate the continuous portion of the size distribution. We have simulated the growth of bodies nearly 8000 km in diameter.